An Evaluation of Microphysics Fields from Mesoscale Model Simulations of Tropical Cyclones. Part I: Comparisons with Observations

ROBERT F. ROGERS AND MICHAEL L. BLACK
NOAA/AOML Hurricane Research Division, Miami, Florida

SHUYI S. CHEN
Department of Meteorology and Physical Oceanography, Rosenstiel School for Marine and Atmospheric Science, University of Miami, Miami, Florida

ROBERT A. BLACK
NOAA/AOML Hurricane Research Division, Miami, Florida

(Manuscript received 22 March 2006, in final form 14 August 2006)

ABSTRACT

This study presents a framework for comparing hydrometeor and vertical velocity fields from mesoscale model simulations of tropical cyclones with observations of these fields from a variety of platforms. The framework is based on the Yuter and Houze constant frequency by altitude diagram (CFAD) technique, along with a new hurricane partitioning technique, to compare the statistics of vertical motion and reflectivity fields and hydrometeor concentrations from two datasets: one consisting of airborne radar retrievals and microphysical probe measurements collected from tropical cyclone aircraft flights over many years, and another consisting of cloud-scale (1.67-km grid length) tropical cyclone simulations using the fifth-generation Pennsylvania State University–National Center for Atmospheric Research Mesoscale Model (MM5). Such comparisons of the microphysics fields can identify biases in the simulations that may lead to an identification of deficiencies in the modeling system, such as the formulation of various physical parameterization schemes used in the model. Improvements in these schemes may potentially lead to better forecasts of tropical cyclone intensity and rainfall.

In Part I of this study, the evaluation framework is demonstrated by comparing the radar retrievals and probe measurements to MM5 simulations of Hurricanes Bonnie (1998) and Floyd (1999). Comparisons of the statistics from the two datasets show that the model reproduces many of the gross features seen in the observations, though notable differences are evident. The general distribution of vertical motion is similar between the observations and simulations, with the strongest up- and downdrafts making up a small percentage of the overall population in both datasets, but the magnitudes of vertical motion are weaker in the simulations. The model-derived reflectivities are much higher than observed, and correlations between vertical motion and hydrometeor concentration and reflectivity show a much stronger relationship in the model than what is observed. Possible errors in the data processing are discussed as potential sources of differences between the observed and simulated datasets in Part I. In Part II, attention will be focused on using the evaluation framework to investigate the role that different model configurations (i.e., different resolutions and physical parameterizations) play in producing different microphysics fields in the simulation of Hurricane Bonnie. The microphysical and planetary boundary layer parameterization schemes, as well as higher horizontal and vertical resolutions, will be tested in the simulation to identify the extent to which changes in these schemes are reflected in improvements of the statistical comparisons with the observations.

1. Introduction

There are many factors that determine a tropical cyclone's intensity and rainfall, such as the magnitude and direction of vertical shear of the environmental wind, upper oceanic temperature structure, and low- and midlevel environmental relative humidity. Ultimately, though, intensity and rainfall are dependent on the magnitude and distribution of the release of latent heat within the core of the storm (Willoughby 1995). The ability to accurately predict the magnitude and distribution of latent heat release is quite challenging, however, and improving our understanding and forecasting

Corresponding author address: Robert F. Rogers, NOAA/AOML Hurricane Research Division, 4301 Rickenbacker Causeway, Miami, FL 33149.
E-mail: robert.rogers@noaa.gov

DOI: 10.1175/JAS3932.1

of intensity and rainfall remains an elusive goal for the operational and research communities. For example, the forecast skill for intensity is only about one-half (one-third) of that for track at 36 h (72 h) forecast time (DeMaria and Gross 2003), while standardized techniques for evaluating tropical cyclone rainfall are only now being developed (Marchok et al. 2007).

Continuing increases in computer power have enabled cloud-scale (grid length ≈1 km), three-dimensional simulations of tropical cyclones to become practically commonplace (e.g., Liu et al. 1997; Zhang et al. 2000; Braun and Tao 2000; Tenerelli and Chen 2002; Rogers et al. 2003). Such high resolution obviates the need for the parameterization of deep convection (e.g., Weisman et al. 1997; Liu et al. 1997), a traditional source of uncertainty in determining latent heating profiles. While convective parameterization is avoided at this resolution, the necessity of parameterizing other processes, such as fluxes of heat, moisture, and momentum from the ocean to the atmosphere, hydrometeor production, conversion, and fallout, and subgrid-scale turbulent mixing, remains. These parameterizations also have uncertainties and deficiencies that may contribute to errors in tropical cyclone intensity and rainfall forecasts. What is needed is a method for evaluating tropical cyclone simulations by comparing them to an extensive set of microphysics observations, including hydrometeor concentrations, radar reflectivity, and vertical motion, that span a variety of storms. Such evaluations can identify biases in the models and point toward ways of improving them. The purpose of this study is to present such an evaluation methodology and illustrate its utility in identifying biases in simulations.

An example of one such bias that is commonly seen in cloud-resolving simulations is model-derived reflectivity that is higher than observed reflectivities. Such a bias has been seen in simulations of environments ranging from high-latitude continental cumulus congestus and hailstorms (e.g., Orville et al. 1984; Farley 1987; Orville and Kopp 1990) to tropical cyclones (e.g., Liu et al. 1997; Rogers et al. 2003). For example, Fig. 1 shows a comparison of a lower fuselage (LF) WP-3D radar sweep from Hurricane Floyd taken at 2259 UTC 13 September 1999 with reflectivity produced by a 1.67-km fifth-generation Pennsylvania State University–National Center for Atmospheric Research (PSU–NCAR) Mesoscale Model (MM5) simulation of Hurricane Floyd from 2300 UTC 13 September 1999. Both the LF radar sweep and the simulation indicate a closed eyewall and multiple rainbands extending out from the southeastern side of the storm. However, the model-derived reflectivities are much higher in both the eyewall and the rainband regions than the radar image. Maximum reflectivities from the radar are 41 dBZ in the eyewall, while many locations within the eyewall and rainbands in the simulation exceed 48 dBZ. Identifying the causes of such differences between simulations and observations may lead to improvements in the simulations and better forecasts of tropical cyclone intensity and rainfall.

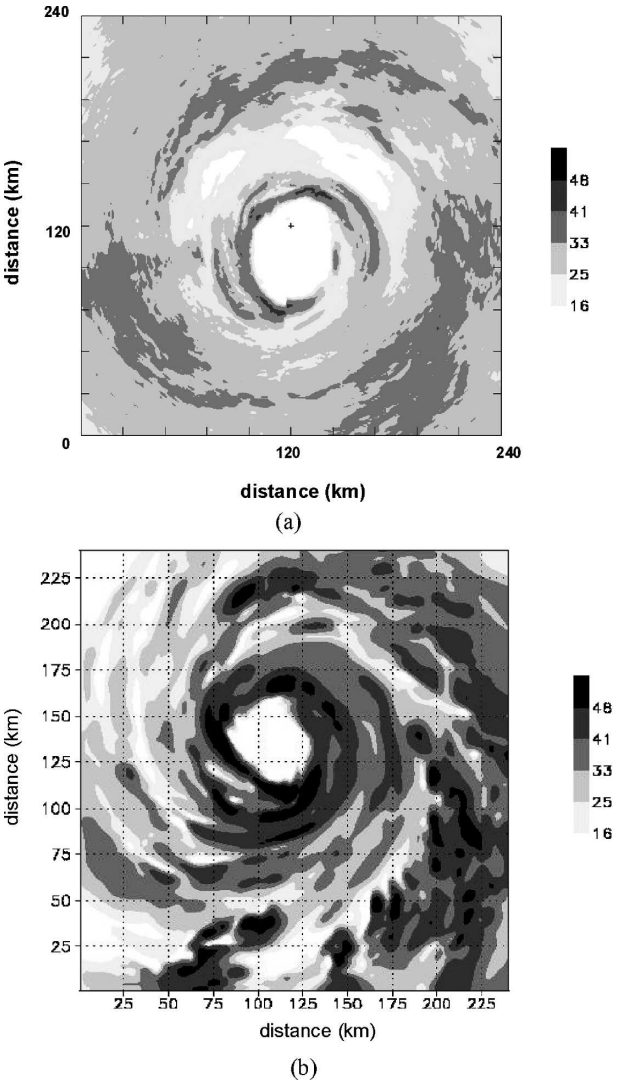

FIG. 1. Comparison of reflectivities (dBZ) from (a) P-3 lower fuselage radar observations at 2259 UTC at 4.2 km and (b) MM5 simulation at 600 hPa for Hurricane Floyd on 13 Sep 1999 [note difference in scales of reflectivity between (a) and (b)].

Many studies have been performed to investigate the structure of tropical cyclones from radar and microphysical probe measurements. These and other observational studies have led to significant improvements in our understanding of the symmetric and asymmetric structure of the tropical cyclone vortex, including the

kinematic and microphysical structures associated with the eyewall and rainbands (e.g., Jorgensen et al. 1985; Marks and Houze 1987; Black and Hallett 1986; Black 1990; Powell 1990a,b; Marks et al. 1992; Barnes and Powell 1995; Black et al. 1996). From these and other studies, a picture emerged of the kinematic structure of a mature tropical cyclone whose symmetric structure is dominated by a primary circulation of high tangential horizontal winds and a secondary circulation consisting of radial inflow in the low levels, ascending motion near the center, and radial outflow aloft. Upward motion is primarily located in the ascending branch of the secondary circulation, that is, the eyewall, and in convective-scale motions embedded within the rainband and stratiform areas of precipitation. In order for a numerical simulation to accurately reproduce the microphysics fields and their variation from region to region within a tropical cyclone, it must adequately resolve the different regions themselves and accurately represent the physical processes that determine the microphysics fields and their distribution as a function of location within the tropical cyclone.

Observations similar to those used in the studies mentioned above often serve as a basis for comparison with output from mesoscale numerical simulations to determine how well these features are represented, but such comparisons are usually limited to simple comparisons of observed radar reflectivity fields with model-derived reflectivity (cf. Fig. 1) and comparisons of near-surface simulated wind fields with comparable analyses. While comparisons of the statistical properties of microphysics fields from cloud-resolving simulations and observations have been performed for tropical convective systems (e.g., Turpeinen and Yau 1981; Yuter and Houze 1995), such comparisons have rarely been performed for tropical cyclone simulations. The evaluation technique presented here seeks to address this deficiency by using Yuter and Houze constant frequency by altitude diagrams (CFADs: Yuter and Houze 1995), along with a new objective technique for partitioning the tropical cyclone into eyewall, rainband, and stratiform regions, to compare the statistics of vertical motion, reflectivity, and hydrometeor concentrations from two tropical cyclone datasets. The first dataset consists of vertical motion and reflectivity from airborne Doppler radar vertical incidence retrievals and microphysical probe measurements collected from tropical cyclone aircraft flights over many years, while the other dataset consists of cloud-scale (1.67-km grid length) tropical cyclone simulations of Hurricanes Bonnie (Rogers et al. 2003) and Floyd (Tenerelli and Chen 2002) using the mesoscale model MM5 (Grell et al. 1994). Comparisons between observations and tropical cyclone simulations using vertical incidence radar data have not been performed before and they could be used to evaluate and improve models by identifying biases in the microphysics fields in the model. By providing a linkage between the vertical motion and hydrometeor fields, this evaluation technique can also be used to improve latent heating profiles retrieved from satellites (e.g., Olson et al. 1999; Tao et al. 2001).

Biases such as those shown in Fig. 1 may have their origins from a number of sources. There may be deficiencies in how the data is processed and compared, for example, data resolution differences, assumptions made in retrieving variables, and algorithms for calculating derived quantities. There may also be deficiencies in the configuration of the model, such as with the model initialization, physical parameterizations (e.g., the planetary boundary layer, surface layer, and microphysical parameterizations), model numerics (e.g., the treatment of horizontal and vertical diffusion), the treatment of ocean mixing and coupling among the atmosphere, ocean, and surface waves, and the horizontal and vertical resolution of the simulation. This study has been divided into two parts. In Part I, the evaluation methodology is presented and statistical comparisons of the microphysics fields are made for control simulations of Hurricanes Bonnie and Floyd with the observational dataset. The sensitivity of the distribution of microphysics fields to changes in some aspects of the model configuration, that is, the physical parameterization schemes and model horizontal and vertical resolution, will be evaluated in a future paper (hereafter Part II) using the methodology described here for the simulations.

2. Methodology

a. Description of observing platforms

1) VERTICAL INCIDENCE RADAR

Vertical motion and reflectivity are calculated using data recorded from Doppler radar systems on each of the two NOAA WP-3D research aircraft. The 3.2-cm Doppler radar is mounted on the tail of the aircraft and scans in a vertical plane normal to the aircraft track. The radar system records reflectivity data that describe the precipitation structure in a vertical plane along the flight track and radial velocities of precipitation particles, toward and away from the aircraft. When the antenna is at vertical incidence (VI), the Doppler velocities are the vertical motions of precipitation particles relative to the aircraft.

The radar, which rotates 10 times per minute, has a 1.9° beam in the plane of rotation and a 1.35° beam

TABLE 1. Name of hurricane, date of flight, intensity information during flight, number (n) of radial legs, average length of radial legs, and the maximum and minimum w from Doppler data during flight.

Storm	Date	Minimum surface pressure (mb)	Maximum wind speed ($m\,s^{-1}$)	Radial legs (n)	Mean leg length (km)	Doppler data	
						Max w ($m\,s^{-1}$)	Min w ($m\,s^{-1}$)
Elena	1 Sep 85	952	60	14	64	13	−11
Elena	2 Sep 85	954	60	14	73	13	−07
Gloria	24 Sep 85	919	70	04	97	24	−21
Emily*	22 Sep 87	957	65	18	65	24	−19
Gilbert	14 Sep 88	892	75	10	96	26	−16
Gabrielle	03 Sep 89	937	60	12	96	14	−11
Hugo	17 Sep 89	930	65	12	107	24	−18
Hugo	18 Sep 89	955	50	06	105	12	−13
Hugo	19 Sep 89	957	45	03	102	12	−12
Hugo	21 Sep 90	934	65	10	103	15	−15
Gustav	27 Aug 90	965	50	06	111	21	−19
Gustav**	29 Aug 90	960	40	30	92	21	−13
Gustav**	30 Aug 90	958	50	12	87	11	−08
Gustav	31Aug 90	959	50	14	94	10	−05
Jimena	23 Sep 91	945	60	8	78	18	−16
Olivia**	24 Sep 94	949	55	28	92	19	−18
Olivia**	25 Sep 94	924	65	32	93	22	−17

* Black et al. (1994) also analyzed these data.
** Both NOAA WP-3D aircrafts flew concurrently.

perpendicular to it, giving a maximum beamwidth of 400 m for altitudes up to 15 km. The WP-3D flies at typical ground speeds of ~125 $m\,s^{-1}$, so VI Doppler data are available at intervals of ~750 m along the flight track. This data is then averaged to 1.5-km horizontal bins to make them comparable to the resolution of the model. In the vertical, the VI data are averaged in 300-m intervals (bins) that extend from just above the sea surface to a height of 15 km. Radial leg lengths (penetrations into or exits out of the eye) vary from 60 to 125 km in length, depending on the flight pattern flown for a particular research mission.

To calculate the vertical winds, the hydrometeor fall speeds and the vertical motions of the aircraft are removed from the raw Doppler radial velocities. The particle fall speeds are determined with bulk formulas using empirically determined reflectivity–fall speed formulas derived in Marks and Houze (1987) and used in Black et al. (1994) and Black et al. (1996). As in Marks and Houze (1987), in the transition layer between regions containing mostly ice particles and regions with rain, the fall speed was interpolated linearly from a rain fall speed at the bottom of the layer to an ice particle fall speed at the top. The aircraft motions are calculated using a combination of inertial navigation equipment and radar altimetry. Since the effects of attenuation of an X-band radar can be large, even over the relative short beam lengths of the VI data, we have employed a two-way attenuation correction factor (Willis and Jorgensen 1981) to the radar data. A lower bound on the reflectivity measurement is used in the aircraft radar data to ensure the vertical velocity estimates are well above the minimum detectable threshold of the radar receiver. These lower bounds are 0 dBZ for flights before 1998 when the prototype Doppler system was used and 5 dBZ for subsequent flights with the current radar system. A similar threshold of 1 dBZ is used to exclude a nearly equivalent amount of low reflectivity values and weak vertical velocities from the model output.

The procedures described above follow the methodology of Black et al. (1996) in which a subset of the VI data described here was used in a statistical study of vertical velocities and radar reflectivity. A summary of the storm names and intensities, and radial leg information for the VI data used in this study, is in Table 1. Observations from nine storms, comprising 233 radial legs, were included in the observational database. The storms that were simulated, Hurricanes Bonnie and Floyd, were not available to be added to the VI database because the tail radar was operating in fore/aft scanning mode (F/AST)[1] during those storms.

2) MICROPHYSICS PROBE

Particle image data from Hurricane Bonnie obtained with the NASA DC-8 aircraft were obtained with the

[1] F/AST is a technique for deducing horizontal wind fields by having the radar antenna alternate between angles up to 20° from perpendicular to the aircraft heading, so there were no radar beams at vertical incidence during those storms.

TABLE 2. List of parameters describing model configurations for Bonnie and Floyd control simulations.

Simulation time	Bonnie:	0000 UTC 22 Aug–0000 UTC 27 Aug 1998 (120 h)
	Floyd:	0000 UTC 11 Sep–0000 UTC 18 Sep 1999 (168 h)
Domain size	Bonnie:	Domain 1: 86 × 86 (3870 km × 3870 km)
		Domain 2: 160 × 160 (2400 km × 2400 km)
		Domain 3: 160 × 160 (800 km × 800 km)
		Domain 4: 160 × 160 (267 km × 267 km)
	Floyd:	Domain 1: 120 × 150 (5400 km × 6750 km)
		Domain 2: 121 × 121 (1815 km × 1815 km)
		Domain 3: 121 × 121 (605 km × 605 km)
		Domain 4: 151 × 151 (252 km × 252 km)
Grid length		Domain 1: 45 km
		Domain 2: 15 km
		Domain 3: 5 km
		Domain 4: 1.67 km
Model top		50 hPa
Number of vertical levels		28
Vertical resolution		50 m in lowest 100 hPa; 1200 m in 200–250-hPa layer
Initial and boundary conditions		AVN 1° fields
		Physical parameterizations
Convective		Kain–Fritsch on domains 1 and 2 (Kain and Fritsch 1993)
		None on domains 3 and 4
Microphysical		Goddard 3-class single-moment bulk scheme on all domains (Tao and Simpson 1993; Lin et al. 1983)
Planetary boundary layer		Blackadar on all domains (Zhang and Anthes 1982) for vertical mixing; K theory using deformation-based eddy diffusivity for horizontal diffusion
		Key parameters for microphysical scheme
Intercept parameter (N_0)		0.08 cm^{-4} (rain)
		1 cm^{-4} (snow)
		0.04 cm^{-4} (graupel)
Particle density (ρ)		1×10^{-3} g cm^{-3} (rain)
		0.1×10^{-3} g cm^{-3} (snow)
		0.4×10^{-3} g cm^{-3} (graupel)
The a and b parameters in fall speed formulation [see Eq. (7)]		
		$a = 2115$ $cm^{0.2}$ s^{-1}; $b = 0.8$ (rain)
		$a = 152.93$ $cm^{0.75}$ s^{-1}; $b = 0.25$ (snow)
		$a = 351.2$ $cm^{0.63}$ s^{-1}; $b = 0.37$ (graupel)

Particle Measuring Systems (PMS) optical array probe (OAP) model 2D-P monoprobe. This probe has a 32-element photosensitive array, measures particles of 0.2–6.4 mm in diameter, and has been discussed in many publications (e.g., Black and Hallett 1986). These data were cleaned of image artifacts using the methods described by Black and Hallett. The 2D-P data were averaged for 6 s. At the DC-8 airspeed of ~205 m s^{-1}, this corresponds to a sample length of ~1.2 km. The 2D monoprobe can easily distinguish snow and ice from rain at sizes >~1 mm diameter. At the same size range, graupel is distinguishable from rain, though with less precision. It is not usually possible to distinguish frozen drops from graupel at any size, and the column/needle crystals are the most easily distinguished from either rain or graupel at all sizes (Black and Hallett 1986). To build a stable size distribution at least 100 or more particle images must be obtained.

b. Model description

The numerical model used is the MM5 (Grell et al. 1994). The MM5 is a fully nonlinear, nonhydrostatic mesoscale model that has a well-demonstrated ability to simulate tropical cyclones (e.g., Liu et al. 1997; Karyampudi et al. 1998; Braun and Tao 2000; Braun 2002; Rogers et al. 2003; Tenerelli and Chen 2002). A detailed description of the model equations and coordinates is given by Grell et al. (1994). For Part I, a control simulation of both hurricanes was performed for comparison with the observations described above. A summary of the configuration in the control simulation is provided in Table 2.

A unique aspect of these simulations is the use of a vortex-following nested grid that allows for long integrations with high resolution in the inner core region of hurricanes (Tenerelli and Chen 2004). The simulations presented here use four domains with grid lengths of 45, 15, 5, and 1.67 km. The inner domains move automatically with the storm, based on the location of the 500-hPa geopotential minimum associated with the storm. High-resolution (30 s) terrain and land-use data are used in the simulations. These fields are read and placed on the fine meshes each time they are initialized or moved. The innermost mesh contains 160 × 160 grid points in the horizontal for each simulation, so the total areal coverage is 267 km × 267 km. This is enough to include all of the inner core and rainbands for each storm entirely within the inner 1.67-km mesh. There are 28 vertical levels in the model with vertical resolution maximized in the lowest 100 hPa (roughly 50-m spacing) and the spacing between levels increasing with increasing height (up to a maximum spacing of about 1200 m). The model initial and lateral boundary conditions for the outermost domain during integration are from the National Centers for Environmental Prediction Aviation Model (AVN, now the Global Forecasting System) one-degree analysis fields. Sea surface temperatures are enhanced by incorporating 9-km Advanced Very High Resolution Radiometer (AVHRR) Pathfinder SST into the SST field.

For the two outer meshes (45 and 15 km), the Kain–Fritsch convective parameterization scheme is used (Kain and Fritsch 1993). This scheme includes a relatively sophisticated cloud model that determines entrainment and detrainment rates as a function of the local environment and includes the effects of downdrafts. Modifications to the Kain–Fritsch scheme include the detrainment of 30% hydrometeors to the resolvable grid and a higher vertical velocity threshold for the initiation of convective clouds, which is more suitable for tropical oceanic conditions. On the inner two meshes, the deepest and strongest convective towers are approximately resolved, so no convective parameterization scheme is used for those meshes.

The Blackadar boundary layer parameterization scheme, which simulates the turbulent mixing of temperature, water vapor, momentum, and cloud water in the vertical, is used on all meshes for the control simulations (Zhang and Anthes 1982). The Blackadar scheme contains two different regimes of turbulent mixing: a stable, or nocturnal, regime and a free-convection regime. The regime is determined by the bulk Richardson number and the Monin–Obukhov length scale. For the stable regime, mixing is determined by local K theory, while for the free-convection regime, vertical transfers of heat, moisture, and momentum are determined by the thermal structure of the whole mixed layer and the surface heat flux. The calculation of surface flux uses a surface energy budget that is based on the force–restore method developed by Blackadar (1979). This budget is dependent on the surface sensible and latent heat fluxes, substrate fluxes, and radiative fluxes. For the runs used here it includes the modification based on Pagowski and Moore (2001) in which different roughness scales for temperature (z_t) and moisture (z_q) are used. This configuration of the PBL scheme has been used successfully to simulate Hurricane Bonnie of 1998 (Rogers et al. 2003), Hurricane Georges of 1998 (Cangialosi and Chen 2004), and Hurricane Floyd of 1999 (Tenerelli and Chen 2002). Horizontal diffusion is specified by a fourth-order scheme that parameterizes horizontal mixing using K theory, with the eddy diffusivity based on the resolvable-scale deformation field following the formulation of Smagorinsky et al. (1965). A simple radiation scheme that allows for the impact of clouds on shortwave and longwave radiation is used (Dudhia 1989).

The microphysical parameterization scheme used in these control simulations is the Tao–Simpson (Tao and Simpson 1993) cloud microphysics scheme for all four meshes. The Tao–Simpson scheme, called the Goddard scheme here, was modified from Lin et al. (1983). It has been used in many tropical cyclone simulations at grid lengths ranging from 1.3 to 81 km (e.g., Liu et al. 1997; Braun and Tao 2000; Davis and Bosart 2002). It is a bulk single-moment three-class ice scheme that contains prognostic equations for cloud water (ice), rainwater (snow), and hail/graupel and it allows for the existence of supercooled water. This scheme includes the processes of condensation/evaporation, freezing/melting, sublimation/deposition, autoconversion (i.e., aggregation) of cloud water (ice, snow) to form rainwater (snow, hail/graupel), collection by rainwater (snow), and accretion.

For the comparisons presented here, high-resolution multiday simulations of Hurricanes Bonnie and Floyd are performed. Hurricane Bonnie was a storm that encountered significant shear for parts of its lifetime, limiting its development to a Category 2 with a minimum central pressure of 954 hPa in the western Atlantic (Pasch et al. 2001). Hurricane Floyd experienced a favorable environment for intensification and nearly reached Category 5 strength over the warm waters just northeast of the Caribbean Sea (Lawrence et al. 2001). The simulation of Hurricane Bonnie is a 5-day simulation with the highest-resolution 1.67-km domain used for the final two days of the simulation. The simulation of Hurricane Floyd is a seven-day simulation with the

1.67-km domain used for the final 4.5 days of the simulation. These simulations reproduce the track and intensity of both storms reasonably well (Fig. 2). A composite database consisting of hourly output during a 24-h period for each simulation is used for comparison with observations. The 24-h time period chosen in each simulation is when the simulated intensity was closest to the observed intensity and the simulated storm was in approximate steady state.

3. Evaluation techniques

a. Statistical comparison methodology

Despite the importance of performing rigorous comparisons between observed and model-produced microphysical properties, only a cursory comparison of gross features between modeled and observed fields have thus far been reported in the literature. Convective processes occur on very small temporal and spatial scales, so it is difficult to have model output and observations at precisely the same location, and at the same time, in the life cycle of any such small-scale feature. The technique of comparing the statistical properties of relevant parameters in both the models and the observations precludes the need for a precise temporal and spatial match and allows for a comprehensive and robust evaluation of the microphysics fields.

One method for comparing model output and observations is to create contoured frequency by altitude diagrams (Yuter and Houze 1995). These diagrams essentially plot the variation of probability distribution functions with height. They provide valuable information about the distributions of parameters, rather than just the means. This technique was used to study the detailed temporal evolution of vertical motion and reflectivity in a midlatitude mesoscale convective system (Yuter and Houze 1995) and the statistical properties of vertical motion and reflectivity from a multitude of tropical cyclones (Black et al. 1996).

For this study the VI observations are used to create the CFADs for comparison with the model output since only the VI data provide the coverage in the vertical necessary to produce the CFADs. To calculate the model-derived CFADs, the model output from the 1.67-km grid is interpolated to a cylindrical grid with a radial resolution of 1.67 km, an azimuthal resolution of 5°, and a vertical resolution of 300 m. The VI data are interpolated to a cylindrical grid with the same azimuthal and vertical resolution but with a radial resolution of 1.5 km. Depending on the ground speed of the aircraft, the resolution of the raw VI data is around 0.75 km, so values of reflectivity and vertical motion from adjacent measurements from the tail radar are averaged together to produce a resolution of 1.5 km. The result is a cylindrical grid with dimensions (r, λ, z) of 165 × 72 × 50, covering a region of nearly 250-km radius. Observations from the radar data normally extend out to about 100–150 km and the outer radii are considered as missing data, while the simulations extend out to about 125-km radius. The centers of the observed storms are calculated from flight-level data and the simulated centers are defined as the location of minimum wind speed at 1.5-km altitude. Each flight typically contains 5–15 radial legs, normally taken along different azimuths (azimuths are defined from north). Each of the legs within a given flight is assigned to a specific azimuth in the cylindrical grid, with the remaining azimuths assigned missing values. The result is an equivalent cylindrical grid of VI radar observations for each flight that can be processed in the same manner as the model output. There are significantly more data points from the simulations than the observations, since

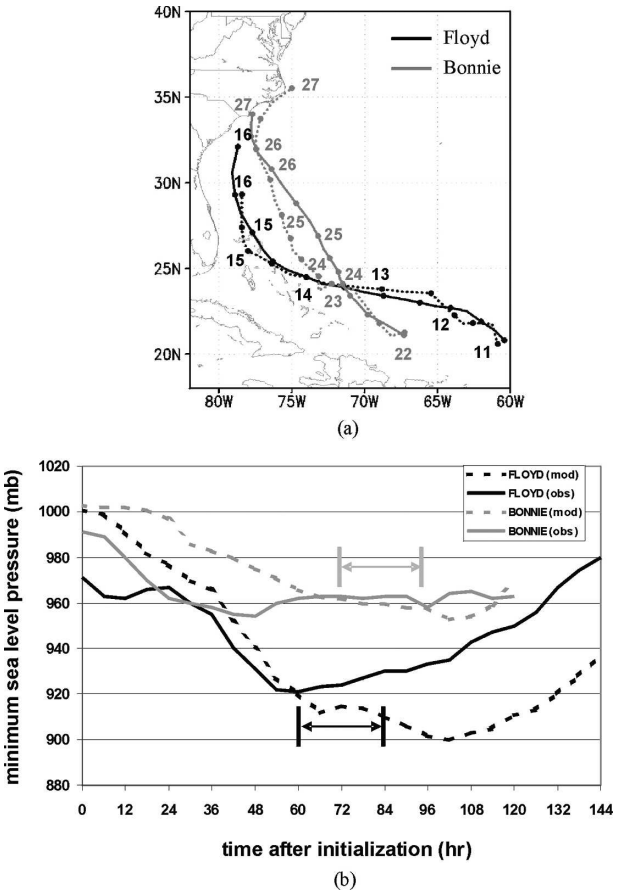

FIG. 2. Plot of observed and simulated (a) track and (b) intensity of Hurricanes Bonnie and Floyd. In both (a) and (b) the solid line is the observed value while the dashed line is the simulated value. Arrows in (b) indicate times used for composites in the simulations.

the output is taken hourly over a 24-h time period for each simulation, while only 5–15 azimuths contain data from each flight. However, the 3500 points in the radar dataset represents our best estimate of the observed statistics, and the discrepancy in data coverage likely does not impact any inferences made in comparing the two datasets. In fact, a random reduction of 50% of the observed sample yields essentially identical results, as in Black et al. (1996).

b. Separation into eyewall, rainband, and stratiform regions

As a part of the comparisons, each of the radials in the cylindrical grids was divided into eyewall, rainband, and stratiform regions, as was done in Black et al. (1996). Unlike the technique in Black et al., which was based on manually evaluating reflectivity patterns from the tail and lower-fuselage radar, this technique is an objective algorithm based on reflectivity and vertical motion fields. The algorithm uses the reflectivity fields to define candidate eyewall, rainband, and stratiform regions and then it uses the vertical motion fields to identify the eyewall and rainband zones within each candidate region. The appendix provides a detailed description of the classification algorithm.

Figure 3 provides examples of the sorting algorithm for two different storms: Hurricane Olivia (1994) from the VI data and the simulation of Floyd. As can be seen from the figure, the scheme does a reasonably good job of differentiating among eyewall, rainband, and stratiform regions, even for storms with structures as different as these. Statistics from the stratification of both the radar and simulation datasets are presented in Table 3. For both observations and simulations, eyewall and stratiform regions make up the bulk of the data. Stratiform regions comprise the majority of points (63% of all points in the observations, 48% in the simulations), while eyewall regions are the second most represented area (24% of all points in the observations, 19% in the simulations). When normalized by area, the preponderance of stratiform points was even more pronounced (69% of total area for observations and 55% for simulations). This reflects the fact that the stratiform regions are typically located radially outward of the eyewall regions, so they span a larger area per unit radial and azimuthal span. The eyewall areal coverage is 16% for the observations and 15% for the simulations, and the rainband areal coverage is 5% for the observations and 11% for the simulations. The areal coverage of the eyewall region in both observations and simulations is nearly identical to the subjectively determined regions in Black et al. (1996), but the areal coverage of stratiform rain is somewhat larger, and the rainband coverage is smaller, in this study. For the rest of this study, discussion will focus on the eyewall and stratiform regions only since they are the most distinct from each other and provide the greatest range of conditions in which a modeling system must perform.

4. Comparisons of simulated microphysics fields with observations

a. Mean profiles

Profiles of mean air updraft and downdraft magnitudes for the observed and simulated eyewall and stratiform regions are shown in Fig. 4. The observed mean eyewall updraft profile shows a relative maximum of about 2.8 m s^{-1} at 5 km and a relative minimum of 2 m s^{-1} in the 6–8-km layer, above the melting layer. This minimum has been seen in other observations of oceanic and tropical cyclone convection (Black et al. 1996; Jorgensen et al. 1994; Jorgensen and LeMone 1989), and it is hypothesized to be caused by water loading and entrainment effects above the melting level that reduce updraft magnitudes. Observed updrafts then increase steadily with height in the upper troposphere, likely caused by updrafts losing their hydrometeors and reaching a maximum as water loading effects are reduced (Black et al. 1996). It could also be partially attributable to the fact that at higher altitudes the radar is capable of measuring fewer points since there are smaller and fewer scatterers at those levels to produce a signal above the radar system's minimum detectable signal. The observed stratiform updraft profile is similar in shape to the observed eyewall updraft profile, but the magnitude of vertical motion is less than in the eyewall, with values that range between 1 and 2 m s^{-1}. Downdrafts in the observations are also much stronger in the eyewall region than in the stratiform region.

In the Bonnie and Floyd simulations, mean updrafts are strongest in the eyewall region and weakest in the stratiform region, similar to the observations. Values of the mean simulated eyewall and stratiform updrafts are about 30%–50% less than the mean observed eyewall and stratiform updrafts, respectively. In contrast to the observations, the mean eyewall downward motion in the simulations is significantly weaker than the mean eyewall upward motion, while in the stratiform region the downward and upward motions are of a comparable magnitude. Another significant difference between the simulations and the observations is that the mean upward and downward motion approaches zero at the surface in the simulations while it remains significant near the surface in the observations, consistent with what was seen in Black et al. (1996). Also, in the simulations the mean upward motion decreases in the upper tropo-

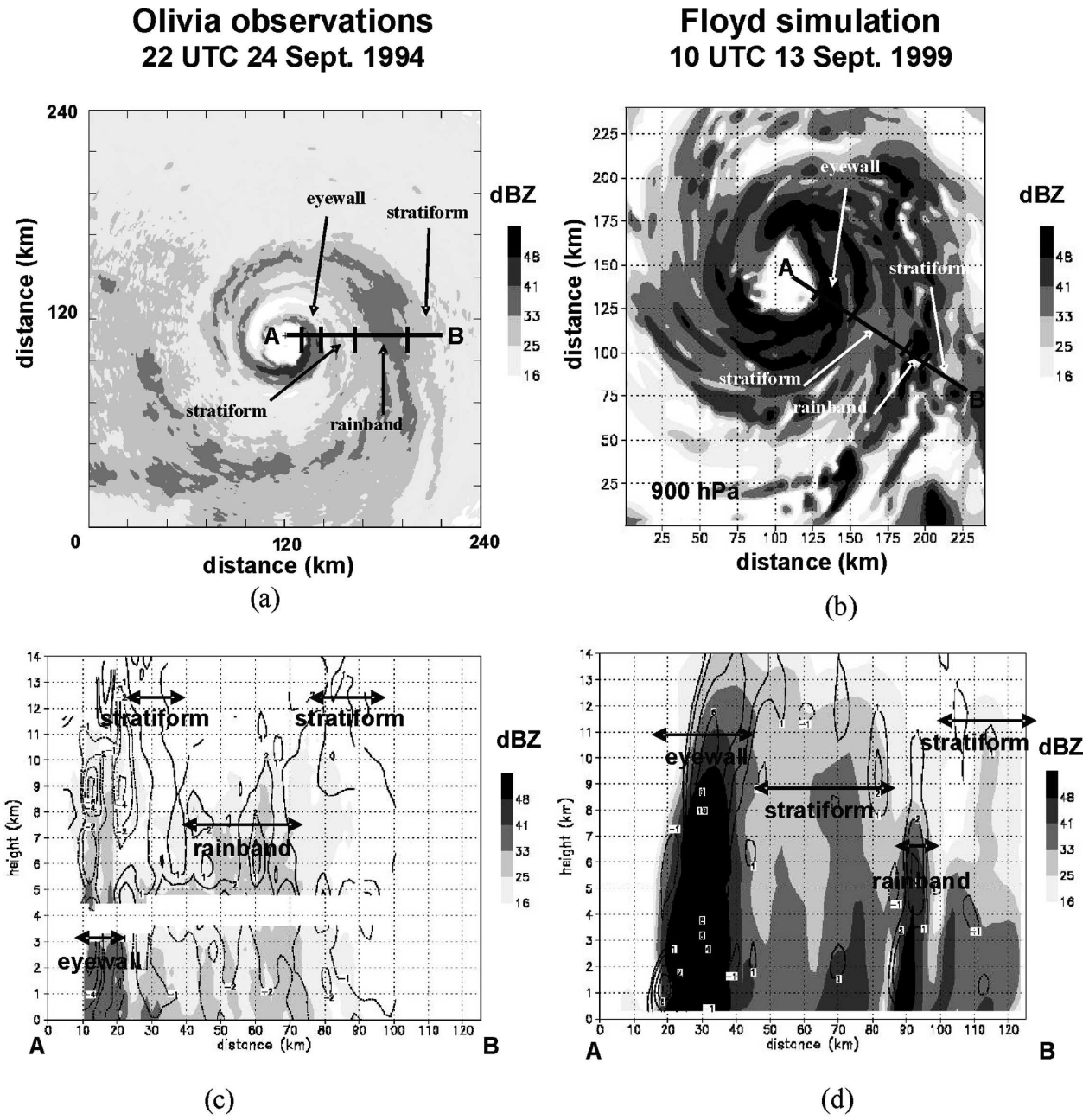

FIG. 3. Examples of regime identification scheme for radar observations of Hurricane Olivia (1994) and simulation of Hurricane Floyd (1999). (a),(b) Plan view reflectivity (shaded, dBZ) images; (c),(d) radius–height cross sections. Areas identified as eyewall, rainband, and stratiform are identified.

sphere for all regions, while in the observations the mean upward motion increases with increasing height.

Profiles of observed and simulated reflectivity for all drafts (updrafts and downdrafts combined) were calculated and are presented in Fig. 5. The observed mean eyewall reflectivity profile (Fig. 5a) shows a structure similar to that seen in Black et al. (1996) for the VI data. Mean reflectivity is around 35 dBZ in the lower troposphere, increasing to a maximum greater than 40 dBZ near the melting level at 4.5 km. Above the melting layer, the reflectivity drops sharply but then shows a secondary peak near 7.5 km. This secondary peak is likely caused by the presence of graupel and frozen drops at the top of vigorous updrafts in the eyewall, evidence of which has been seen at altitudes as high as 12 km (Black et al. 2003). Above this secondary peak,

TABLE 3. Characteristics of regions in VI (dataset from Table 2) and model (Bonnie and Floyd simulations) data.

	Number of occurrences	Percentage of total occurrences	Contribution of region to total area (%)
		VI data	
Eyewall	836	23.5	15.5
Rainband	137	3.9	4.7
Stratiform	2231	62.7	68.6
Other	352	9.9	11.2
		Model data	
Eyewall	49 384	18.6	14.8
Rainband	21 273	8.0	10.7
Stratiform	127 761	48.0	55.1
Other	67 760	25.4	19.4

the reflectivity continues to decrease, falling below 20 dBZ at 11 km. Values of reflectivity for the stratiform region are lower than the eyewall with mean reflectivities of around 30 dBZ in the lower troposphere dropping below 20 dBZ at 6.5 km and a bright band near 4–5 km.

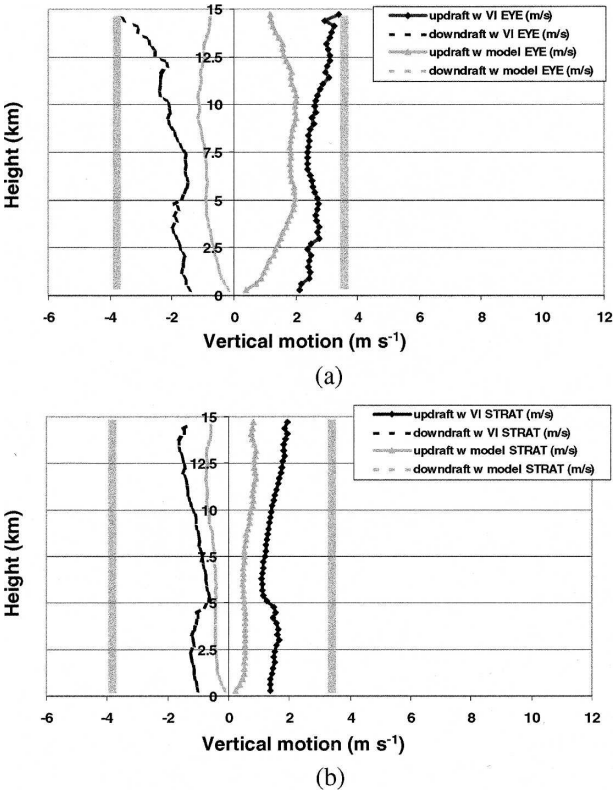

FIG. 4. Profiles of observed and simulated mean updrafts and downdrafts (m s^{-1}) sorted by (a) eyewall and (b) stratiform regions. Vertical shaded bars denote those levels where differences are significant at the 99% confidence level.

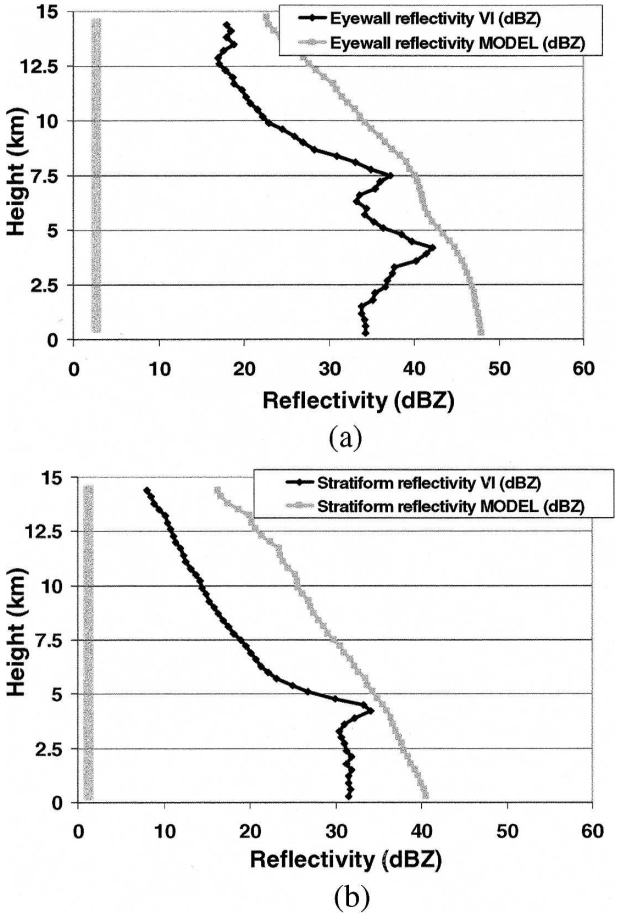

FIG. 5. Profiles of Doppler-derived and simulated reflectivity (dBZ) for all storms sorted by (a) eyewall and (b) stratiform regions. Vertical shaded bars denote those levels where differences are significant at the 99% confidence level.

The simulations show the bias toward high reflectivity discussed previously. Simulated mean eyewall reflectivities are much higher than observed, with low-level values approaching 48 dBZ. There is no peak in mean reflectivity at the melting level, only a slight change in slope with height between 4 and 5 km. The reason for the absence of a reflectivity peak below the freezing level in the simulations is likely that the model does not account for frozen aggregates with liquid water coating the surface, the cause of most bright bands in radar observations (Ferrier et al. 1995). Above this level the reflectivity continues to decrease but not as rapidly as the observed reflectivity. Above 12 km the reflectivity does begin to decrease rapidly, but it remains significantly higher than the observed reflectivity at all heights up to 15 km. The high reflectivity bias seen in the model values could be at least partially attributable to the way in which reflectivity is calculated in the model (see section 5b).

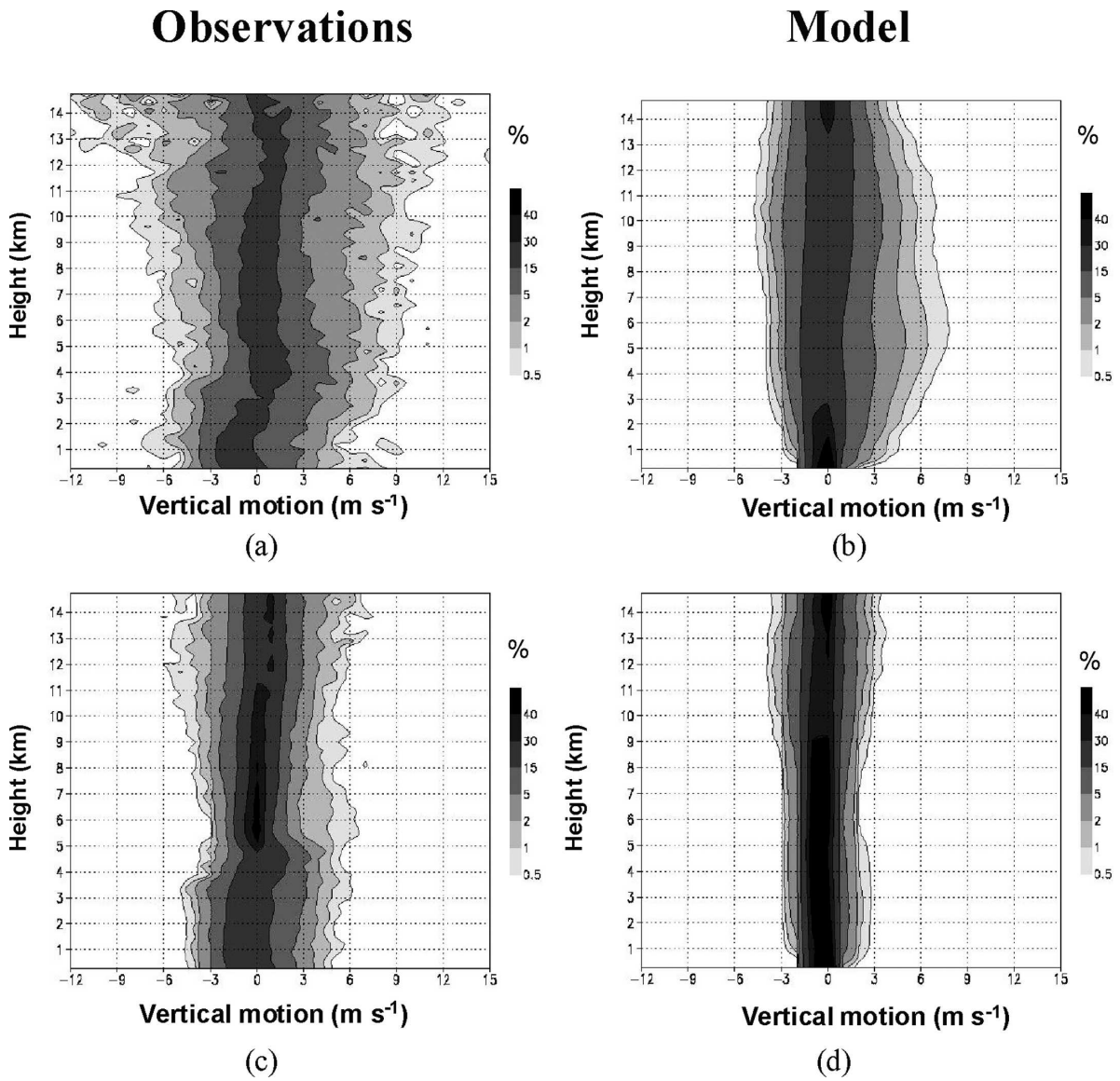

FIG. 6. Contoured frequency by altitude diagrams (CFADs; shading, %) of (a),(c) Doppler-derived observations and (b),(d) model simulated vertical motion for all storms sorted by (top) eyewall and (bottom) stratiform regions.

b. Distributions

To compare the distributions of the various fields rather than just their means, CFADs (see section 3a) are calculated. Figure 6 shows CFADs of vertical motion for the observations and simulations sorted into eyewall and stratiform regions. As in Black et al. (1996), the majority of vertical motions are weak ($|w| < 2$ m s^{-1}), but a small fraction (1%–2%) of up- and downdrafts exceed 6 m s^{-1}. The observed distributions of vertical motion are broader for the eyewall region than for the stratiform region. Values of observed vertical motion in the eyewall range from -6 to 9 m s^{-1} below the melting level. Observed vertical motions remain large just above the surface, and the distributions are fairly constant with height below the melting level. Above the melting level they broaden with height, indicating strong peak up- and downdrafts aloft (± 12 m s^{-1}) at 13 km. The maximum frequency (i.e., mode) of observed vertical motions is slightly negative in the lowest 2 km, but it becomes near zero or slightly positive above there. Above 9 km the mode of vertical motion is clearly upward, reflecting the loss of hydrometeors and reduction in water loading in the upper levels, similar to what was seen in the observed mean eyewall updraft profile in Fig. 4a. The observed stratiform

CFAD (Figs. 6c and 6e) is narrower than the observed eyewall CFAD. Peak up- and downdrafts are ± 5 m s^{-1} below the melting level and the distribution narrows just above it. In the upper troposphere the distribution broadens with height. Modal vertical motions are about zero below 10–11 km and become positive above there. In contrast to the observations, the simulated vertical motion CFADs show a narrower distribution of vertical velocities. The majority of simulated up- and downdrafts are weak, similar to the observations, but the maxima are weaker than the observed values. In the eyewall (Fig. 6b), values in the lower troposphere range from -3 to 4 m s^{-1}. In both eyewall and stratiform regions in the simulations, the vertical motions approach zero near the surface, in contrast to the observations. The range of upward motions increases with increasing height up to the melting level at 5–6 km at which point the top 1% of points have upward motion of about 8 m s^{-1}. Above the melting level the peak values decrease, but then there is another relative maximum at about 10 km. Above 10 km, the distribution narrows, in contrast to the observed distributions. The modal values in the eyewall are about zero in the lowest 2 km and become negative up until 8 km, above which it becomes slightly positive. As in the observations, the stratiform distribution of vertical velocity (Fig. 6f) is narrower than the eyewall distribution, with values ranging between -3 and 3 m s^{-1} for nearly the entire depth of the troposphere. The distribution of vertical motion is nearly constant with height in the stratiform region. The modal vertical motion is slightly negative from the surface to 12–13 km where it becomes zero. In both eyewall and stratiform regions of the simulations, the downdrafts rarely exceed 4 m s^{-1}.

CFADs of reflectivity are shown in Fig. 7. The observed eyewall CFAD is the most broadly distributed, with peak values around 45 dBZ in the lowest 2 km and peak values near 30 dBZ at 12 km for the top 1% of points. In both eyewall and stratiform regions, the distribution shows a slight decrease in reflectivity with height in the lowest 1–2 km, followed by an increase with height up to the melting level as warm rain processes apparently cause an increase in hydrometeor mixing ratios. Also in both regions, the distributions show a maximum in reflectivity at the melting level, followed by a sharp drop-off above the melting level. The reflectivity peak at the melting level in the eyewall sample is indicative of a bright band, suggesting that there is some stratiform precipitation in the eyewall. Hurricane eyewalls often contain substantial areas of stratiform precipitation, particularly in the weak reflectivity side of asymmetric storms. Stratiform rain is also frequently observed adjacent to and radially outward from the convective portion of the eyewall inner edge, in an area that would be classified as an eyewall by partitioning schemes like that shown here and elsewhere (e.g., Black et al. 1996). The rate of decrease is larger for the stratiform regions than for the eyewall because the eyewall contains stronger updrafts that can transport hydrometeors to higher levels before they fall out (Black et al. 1996). The modal values of reflectivity are different for each region as well, with values of 30 dBZ in the lower troposphere in the eyewall region and 20–25 dBZ in the stratiform region.

In the simulations (Figs. 7b and 7d), the eyewall CFAD shows a broader distribution of reflectivity than the stratiform CFAD, similar to the observations. The high reflectivity bias mentioned in the introduction is clear in these figures. Values approach 60 dBZ for the top 1% of points and the mode in the lowest 3 km is around 40–45 dBZ for the eyewall and 25–30 dBZ for the stratiform region. Similar to the profiles of mean reflectivity (cf. section 3a), no bright band is evident in the simulated CFADs. One final significant difference between the CFADs of observed and simulated reflectivity is the fact that the decrease with height of reflectivity above 5 km is much smaller in the simulations than in the observations. The ramifications of this difference are discussed later.

c. Correlations

A scatterplot of flight-level vertical motion and probe measurements of hydrometeor mixing ratio for a mixed convective and stratiform portion of a NASA DC-8 flight into Hurricane Bonnie on 26 August 1998 is compared with a scatterplot from an equivalent "flight level" measurement from the model (Fig. 8). As indicated by the linear regression lines fit to each distribution (Fig. 9), there is virtually no relationship between observed vertical motion and mixing ratio at 9.9 km, while the simulated fields show a much stronger relationship. The variance explained by the regression line in the observations is less than 1%. In the model, nearly 58% of the variance is explained by the linear fit. A Student's t test was performed on the two datasets to determine the level of statistical significance at which the correlation coefficient (r) can be considered to be nonzero. There is only a 50% confidence that r is nonzero in the observed distribution, while there is a 99.8% confidence that r is nonzero in the simulated distribution, indicating a much higher confidence in the strength of the relationship in the simulation.

Figure 10 shows comparisons of the VI and model mean reflectivity stratified by vertical velocity as a func-

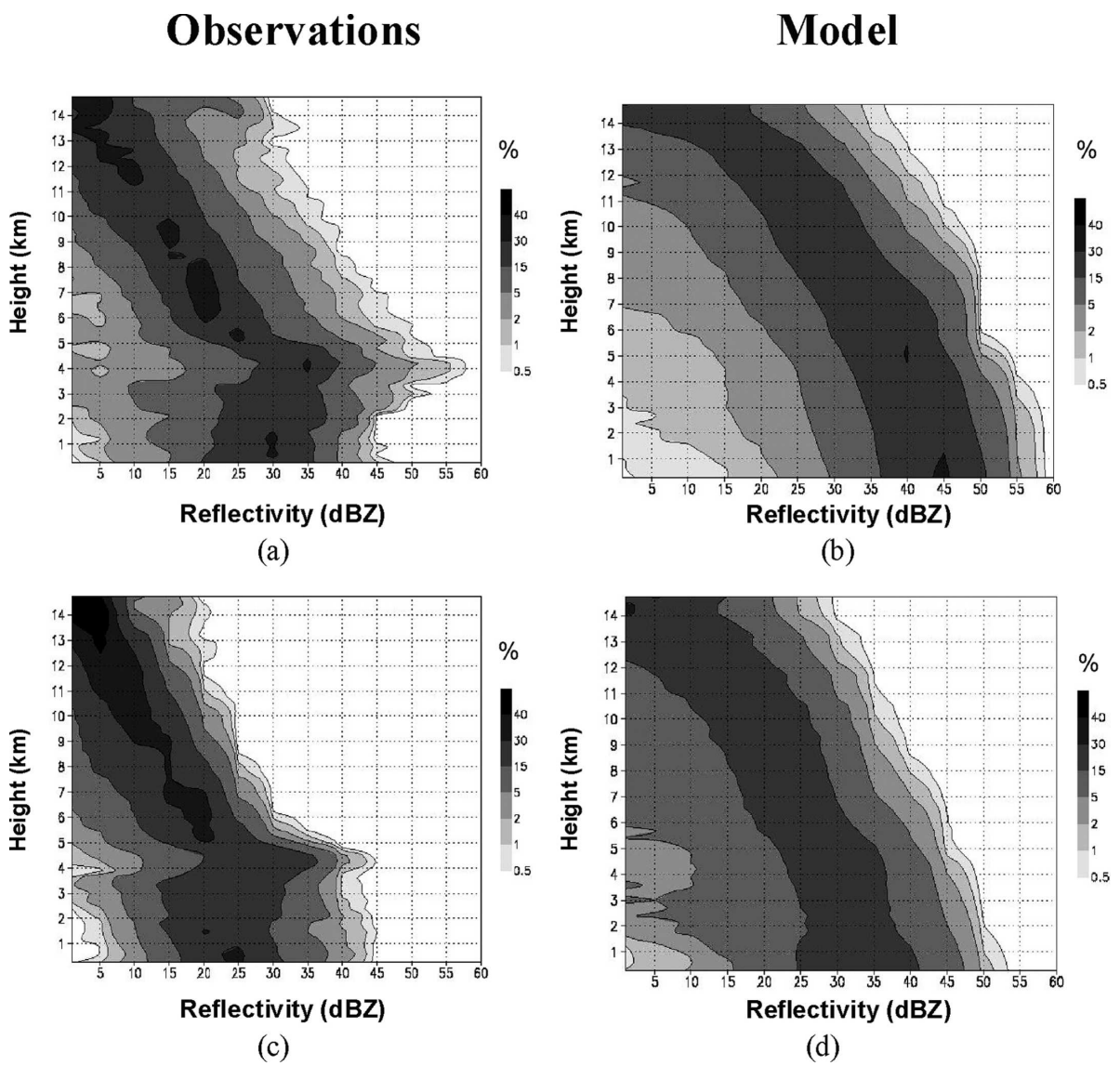

FIG. 7. As in Fig. 6 but for CFADs (shading, %) of reflectivity.

tion of height. Such a comparison provides an independent comparison of the relationship between vertical velocity and hydrometeor concentration (as manifested by the reflectivity field) and it provides a larger sampling volume than probe measurements for comparing the relationships between observed and simulated fields. Similar to the scatterplots in Fig. 9 for hydrometeor mixing ratio, there is a suggestion of a weak relationship between observed reflectivity and vertical motion. Between 3-km and 5-km altitude, observed reflectivity values increase slowly as upward motion increases from 0 to 9 m s^{-1} (e.g., increasing from 37 dBZ at 0 m s^{-1} to 47 dBZ at 6 m s^{-1} at the 4-km level). Above the melting level, between 7-km and 12-km altitude, there is again a weak relationship between vertical motion and reflectivity for both up- and downdrafts. The relationship between vertical motion and reflectivity is much stronger for the simulations, however. The slope of the relationship is very pronounced for the weak vertical motions (i.e., between -2 and 2 m s^{-1}), and there is a noticeable slope even for the vertical motion values exceeding 9 m s^{-1}. Although the uncertainty of fall speed estimates in heavy rain or in strong mid- and upper-level updrafts [$\sim$2 m s^{-1} according to Black et al. (1996)] in the VI data could account for some of the scatter in the correlations for weak updrafts (<2 m s^{-1}), this could not account for the weak correlations between the stronger updrafts (>3 m s^{-1}) and radar reflectivity in the observations. The differences in the strength of the relationship between

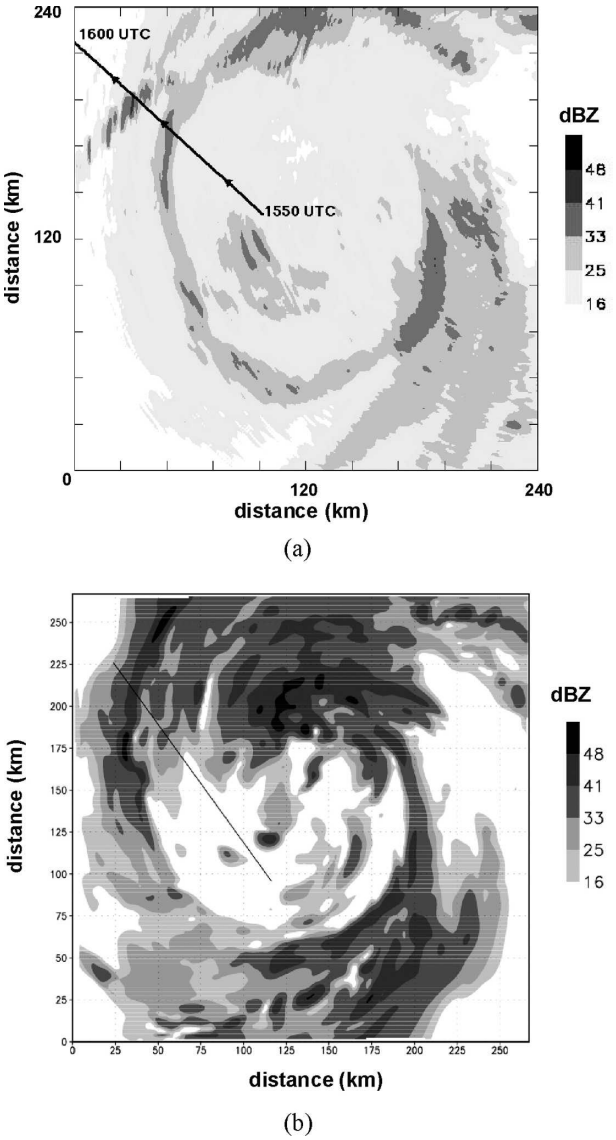

FIG. 8. Reflectivity fields and leg location used to construct scatter diagram in Fig. 9. (a) P-3 LF reflectivity in Bonnie at 1545 UTC 26 Aug, altitude 3.7 km, and (b) model-derived reflectivity at 650 hPa for Bonnie simulation at 1600 UTC 26 Aug. Lines in (a) and (b) indicate locations where flight-level values of vertical motion and hydrometeor concentration were taken at 9.9-km altitude.

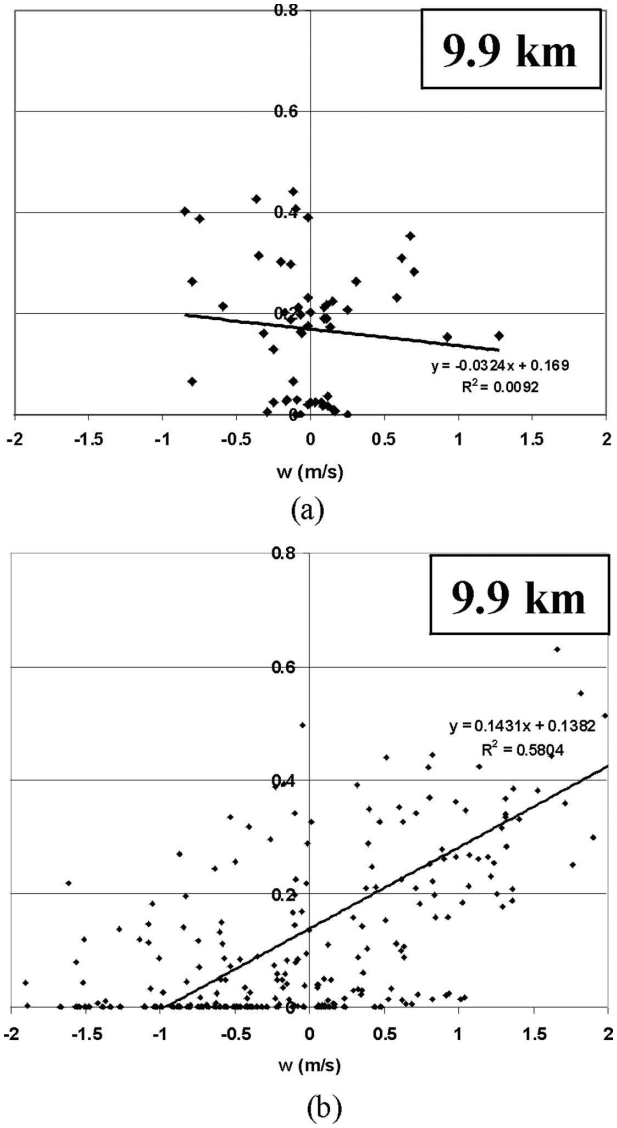

FIG. 9. Scatterplots of flight-level vertical motion (m s^{-1}) and hydrometeor concentrations (g kg^{-1}) at 9.9 km for (a) observations and (b) model simulation of Bonnie.

vertical motion and reflectivity in the observations and simulations shown in Fig. 10 are consistent with the differences in the probe data.

5. Discussion

a. Summary of comparisons between observations and simulations

The comparisons presented here show that the model reproduces many of the gross reflectivity and vertical velocity features seen in the observations. For example, the majority of the vertical motion is weak in all regions for both the observations and simulations, profiles of both observations and simulations show increasing vertical motion and decreasing reflectivity with height above the melting level, and the upward motion is strongest; the distributions of vertical motion and reflectivity are broadest in the eyewall and weakest and narrowest in the stratiform regions. Despite these similarities, there are many significant differences between the observations and the simulations that suggest notable biases in the simulations:

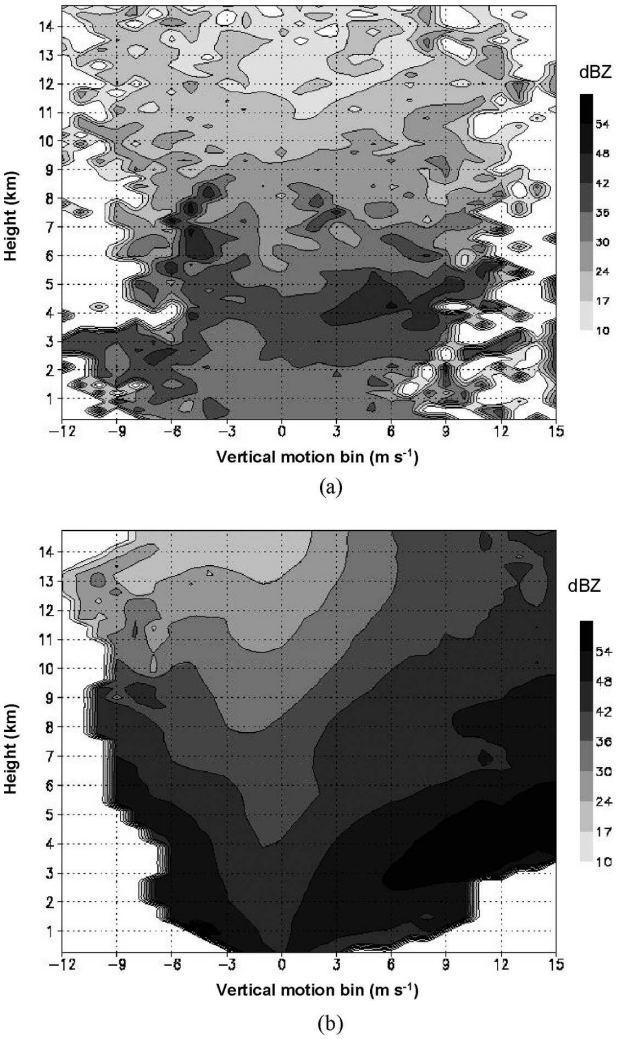

FIG. 10. Mean eyewall reflectivity (shading, dBZ) stratified by (a) Doppler-derived observations and (b) model-derived vertical motion bins for all storms.

- Mean updrafts and downdrafts are weaker in simulations than in the observations, and magnitudes of simulated mean reflectivity are higher than the observations throughout the troposphere
- Mean updrafts- and downdrafts increase in magnitude with height in observations and decrease with height in simulations
- Mean and peak values of updrafts- and downdrafts approach zero near the surface in the simulations and remain large just above the surface in the observations
- Reflectivity decreases much more slowly with height above the melting level in the simulations than it does in the observations
- Distributions of vertical motion (reflectivity) are narrower (broader) for the simulations than for the observations
- Modal and maximum vertical motion (reflectivity) is lower (higher) in simulations
- Distribution of vertical motion narrows with height in the simulations and broadens with height in the observations
- Correlation between vertical motion and hydrometeor mixing ratio/reflectivity is much higher in simulations than in the observations.

b. *Possible causes of differences between observations and simulations*

1) DATA PROCESSING DIFFERENCES

There are many possible sources of difference between the observed and model-simulated fields, ranging from differences in how the data are processed and compared to deficiencies in the physical parameterizations in the model. For Part I, attention will be focused on the differences that are primarily due to different data processing methods. For example, a consistent result that arises from the comparisons between observations and simulations is that the magnitude of the radar reflectivities calculated from the model is higher than those measured by the radar. Reflectivity in the model is calculated using the total mass content of individual constituent species and adding their reflectivity values together to yield a total reflectivity value (Smith et al. 1975; Fovell and Ogura 1988; Braun and Houze 1994), assuming 100% Rayleigh backscattering for each of the constituent species:

$$Z_e = 720\alpha\kappa N_{0x}\left(\frac{\rho_x}{\rho_w}\right)^2[(\pi\rho_x N_{0x}/\rho q_x)^{1/4}]^{-7}, \qquad (1)$$

where

Z_e = equivalent reflectivity (mm^6),
α = ratio of backscattering coefficients for the reflecting particles and water (taken as 1 for rain and 0.213 for precipitating ice),
κ = conversion factor from m^3 to mm^6 m^{-3} (equal to 10^{18}),
N_{0x} = intercept parameter of species x (m^{-4}),
ρ_x = density of particle (kg m^{-3}; frozen or liquid depending on type of particle being considered),
ρ_w = density of water (kg m^{-3}),
ρ = density of air (kg m^{-3}),
q_x = mixing ratio of species x (i.e., rain, snow, graupel; kg kg^{-1}).

Equation (1) can be rewritten as

$$Z_e = \kappa C(\rho q_x)^{1.75}, \qquad (2)$$

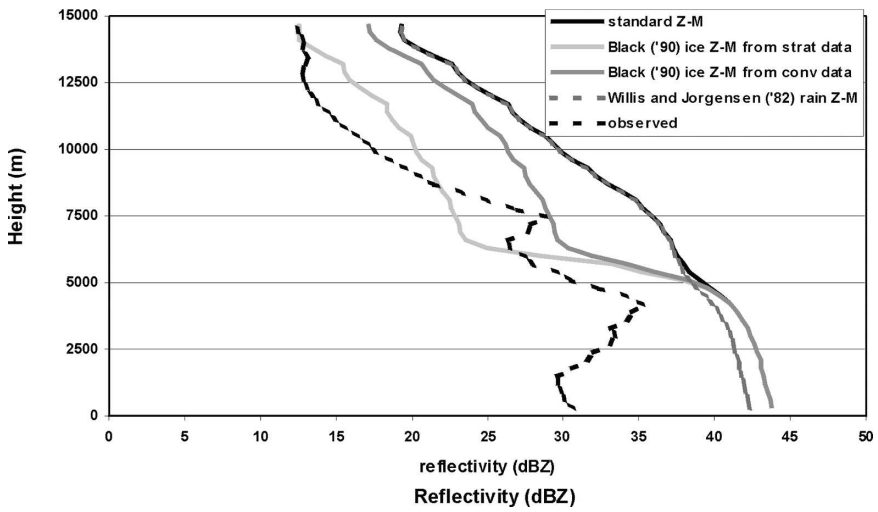

FIG. 11. Profiles of mean reflectivity (dBZ) for all regions using different Z–M relations.

where

$$C = \frac{720\alpha N_{0x}}{(\pi\rho_x N_{0x})^{1.75}}\left(\frac{\rho_x}{\rho_w}\right)^2. \quad (3)$$

From this relationship it can be seen that the reflectivity calculated in the model is dependent on the assumed intercept parameter (N_0), assumed particle density (ρ_x), and simulated mixing ratio (q_x) for each species. The reflectivity in the model is thus calculated by using the total mass content of each individual constituent (precipitating) species and adding their reflectivity values together to yield a total reflectivity value.

Equation (2) is essentially a reflectivity–mass (Z–M) relationship of the form

$$Z = aM^b. \quad (4)$$

For the model calculations used here, the value of the a (b) parameter is 1228 (1.75), 5810 (1.75), and 20417 (1.75) for snow, graupel, and rain, respectively. When there is a mixture of particle types at a grid point, the effective Z–M relation is a mixture of the constituent Z–M curves. The values of these model parameters contrast significantly with equivalent Z–M relations determined empirically from probe measurements in a variety of hurricanes (Willis and Jorgensen 1981; Black 1990). For example, the values of the a (b) parameter for locations above the melting level were estimated to be 915 (1.51) and 219 (1.4) for a predominantly convective and stratiform storm, respectively (Black 1990), while the a (b) value below the melting level in another hurricane was estimated to be 14 632 (1.4482) (Willis and Jorgensen 1981). To test the significance of using a different model Z–M relation to explain the bias in the model-derived reflectivity, model reflectivities are recalculated using the empirically derived relations from Willis and Jorgensen (1981) for levels below the melting level and Black (1990) for levels above the melting level. Figure 11 shows reflectivity profiles for all points from the Floyd and Bonnie simulations using these alternate Z–M relations, as well as the reflectivity for all points in the VI database. Using alternate Z–M relations does produce significant differences in the reflectivity profiles above the melting level. For example, the reflectivity is reduced by nearly 10 dBZ above the melting level when using a relation characteristic of a convective storm and 15 dBZ when using a relation taken from a stratiform storm. In both of these modified profiles, however, the reflectivity decrease with height above 7.5 km is still less than the observed decrease with height. Using the modified rain relation does reduce the reflectivity about 2–3 dBZ, but this value is still much higher than the observed reflectivity. It must also be emphasized that using different Z–M relations implicitly means using different assumptions regarding intercept parameter and particle density [cf. Eq. (3)]. To gain a true understanding of the impact of varying these parameters, they must also be changed in the scheme itself and the simulation must be rerun using these new values. Such tests will be performed in Part II.

Another consistent difference between the observations and the simulations is that the simulated vertical motions are weaker than the observed vertical motions. There are many uncertainties in the calculation of the vertical velocity from both the observations and the simulations, which may explain these differences. One uncertainty in comparing the retrieved and the simulated vertical motion fields lies in the estimates of fall speed used to derive the air vertical motions. As men-

tioned in section 2, the vertical motions from the radar are determined by subtracting estimates of fall speeds from measured velocities of scattering hydrometeors. This can be expressed by the relation

$$w_{\text{air}} = w_{\text{dop}} - w_{\text{fs}}, \tag{5}$$

where w_{dop} is the actual measured Doppler velocity of the hydrometeors, w_{fs} is an estimate of the fall speed of the hydrometeors [derived using radar reflectivity here as in Black et al. (1996)], and w_{air} is the vertical air motion that is compared with the vertical velocity from the simulations. Errors in comparing the retrieved and the simulated vertical motions can arise when there are errors in the assumed values of w_{fs}, which can result from uncertainties in the fall speeds of particular hydrometeor species and the partitioning of a given radar reflectivity among snow, graupel, and rain concentrations.

To compare vertical motions independent of errors in fall speed estimates, Fig. 12 shows CFADs of eyewall w_{dop} and w_{fs} from the radar and simulation databases along with the CFADs of w_{air}. Expressions for w_{dop} from the simulations are derived by first calculating w_{fs}, which is the fall speed weighted by reflectivity for each of the species present at a given grid point:

$$w_{\text{fs}} = \frac{\sum_x w_{\text{fs},x} Z_x}{\sum_x Z_x}, \tag{6}$$

where Z_x is the reflectivity for each species x calculated from Eq. (1) and $w_{\text{fs},x}$ is the fall speed for each species, calculated from (e.g., Lin et al. 1983; McFarquhar and Black 2004)

$$w_{\text{fs},x} = \frac{c\Gamma(4 + d)}{6\lambda^d}. \tag{7}$$

The terms c and d are constants. The value of c is 2115 $\text{cm}^{0.2}\ \text{s}^{-1}$ for rain, 152.93 $\text{cm}^{0.75}\ \text{s}^{-1}$ for snow, and 351.2 $\text{cm}^{0.63}\ \text{s}^{-1}$ for graupel and the value of d is 0.8 for rain, 0.25 for snow, and 0.37 for graupel. The value for w_{fs} from Eq. (6) is then added to the model-produced vertical air motion to derive w_{dop}. As can be seen from Fig. 12, the fall speeds used in the estimates for the radar retrievals and those used in the simulations show a similar distribution. Below the melting level the modal values for the rain fall speeds are around 6 m s^{-1}, with peak values ranging between 3 and 9 m s^{-1}. In the upper troposphere, the modal values for the snowfall speeds are around 1–2 m s^{-1}, with a much smaller range of possible values between 0 and 3 m s^{-1}. For the altitudes near the melting level, that is, between 4 and 8 km, peak fall speeds used in the observations are higher than in the simulations. Some of this difference may reflect errors in the estimate of graupel fall speed in the VI data (e.g., an overestimate of the depth of the layer over which the blending of rain and ice fall speeds, see section 2a) or an underestimate of graupel fall speed in the simulations. Despite these differences in the fall speeds around the melting level, the resultant w_{dop} fields show the same relationship between the observations and the simulations as the w_{air} fields do. Modal values of w_{dop} are comparable between the datasets, the observed fields of w_{dop} show a broader distribution at all altitudes than do the simulated fields of w_{dop}, and the distribution of observed w_{dop} continues to broaden with height in the upper troposphere compared with the simulated distribution of w_{dop}, which narrows with height. Since the differences in the w_{dop} fields between the observations and the simulations are the same as those for the w_{air} fields, then the uncertainties in the estimates of fall speed are likely not a significant contributor to differences between the observed and simulated fields of vertical motion.

Another possible explanation for why the simulated vertical motion is less than the observed vertical motion is that the resolution of the model is coarser than the effective resolution of the radar data (1.67-km square grid length for the model versus a maximum 400-m measurement averaged to 1.5 km for the VI data). Also, since the model can really only resolve features on the order of 4–8 Δx or greater, where Δx is the grid length, then the minimum size of the up- and downdrafts resolved in the model are on the order of 6–12 km. To address this question, CFAD comparisons of eyewall w_{dop} for both the VI data and model output are averaged to $8\Delta x$ resolution (Fig. 13) in an attempt to compare fields that are better resolved. Not surprisingly, averaging down to this resolution decreases the magnitude of the strongest drafts in both the retrieved and the simulated vertical motion fields. For example, the top 0.5% of w_{dop} values from the VI data at 10 km decrease from 8.5 to 6 m s^{-1} after averaging to $8\Delta x$, while the top 0.5% of values from the model output decrease from 4.5 to 3 m s^{-1}. While averaging to this resolution impacts the distributions of each dataset, the relationship between the two datasets remains essentially the same: namely, peak values of vertical motion are still stronger in the observations compared with the simulations, and the distributions broaden with height above the melting level in the observations while they narrow with height in the simulations. Thus averaging to $8\Delta x$ resolution does not significantly alter the relationship between the observed and simulated vertical velocity fields. Furthermore, resolution differences likely do not explain differences in the correlations be-

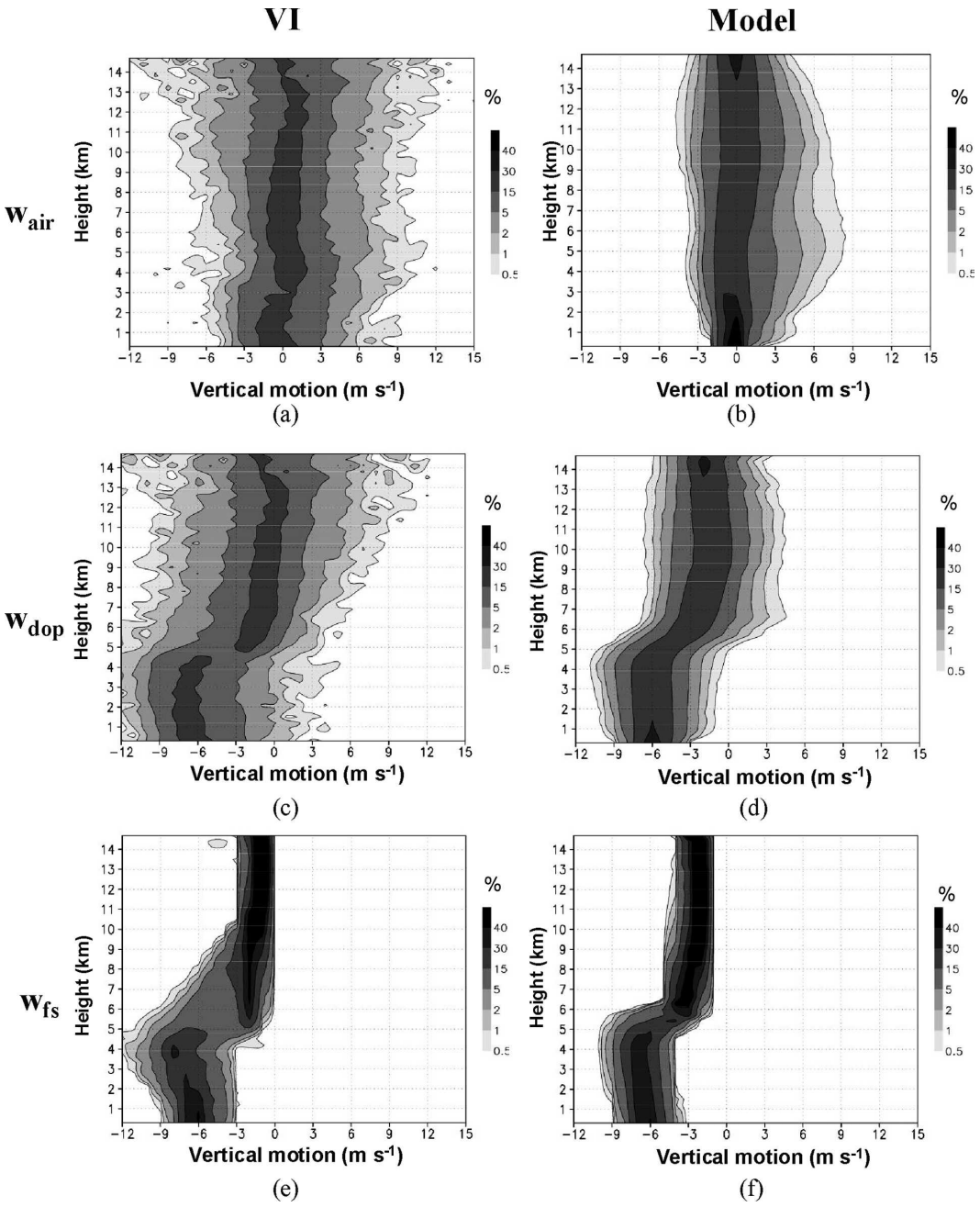

FIG. 12. CFADs of eyewall w_{air}, w_{dop}, and w_{fs} for (a),(c),(e) VI data and (b),(d),(f) simulations.

tween the vertical motions and hydrometeor mixing ratios and reflectivities.

2) DEFICIENCIES IN THE MODEL

Despite the possible sources of differences between the observations and the simulations discussed above (e.g., *Z–M* relation differences, fall speed assumptions, resolution differences), many of the differences are likely to be at least partially attributable to deficiencies in the configuration of the model, whether by insufficient resolution or deficient physical parameterizations. These possible sources of error are briefly discussed below, and they will serve as motivation for the sensitivity tests that will be shown in Part II.

The microphysical parameterization makes several key assumptions that may impact the distribution of hydrometeors and the vertical velocities (e.g., McFarquhar and Black 2004). Errors in the formulation of

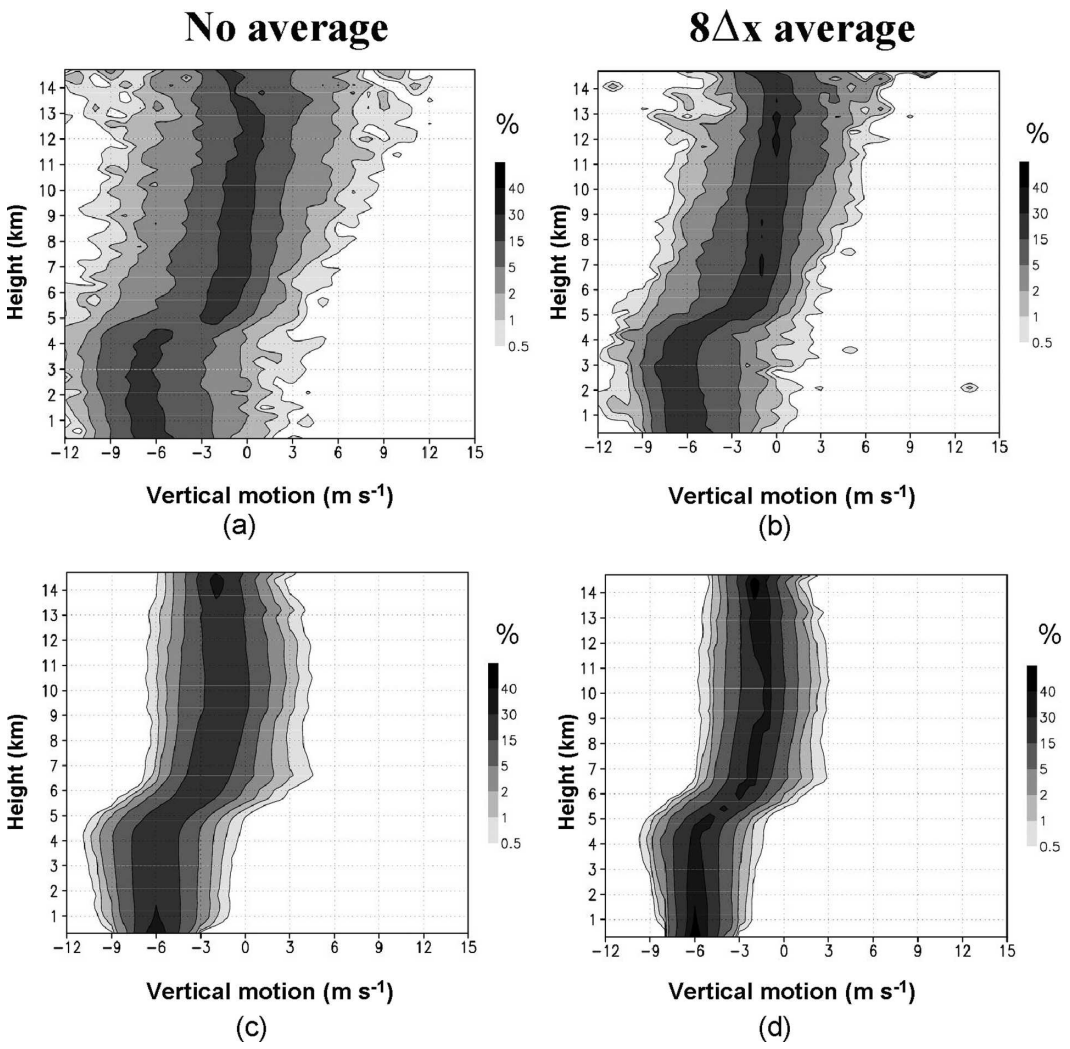

FIG. 13. CFAD comparisons of eyewall w_{dop} (shading, %) for (a),(b) VI data and (c),(d) Bonnie and Floyd model simulations. Raw gridded fields are shown in (a) and (c); gridded fields averaged to $8\Delta x$ resolution are shown in (b) and (d).

graupel fall speed, for example, may impact the amount of water loading and result in inaccurate updraft magnitudes, hydrometeor concentrations, and correlations between vertical motion and hydrometeor concentration. Uncertainties in the size distributions will lead to uncertainties in the mass-weighted mean diameter, collection efficiency, and fall speed. Errors in hydrometeor production and conversion terms may also lead to errors in the amount and distribution of hydrometeors in the simulation. The representation of hydrometeor populations as discrete species, each with their own unique fall speed formulations, may be a source of error in the model. This is one limitation that is magnified with single-moment bulk schemes, since they prescribe size distributions for each species as a function of either slope or intercept parameter. Using a higher-moment bulk scheme or a bin scheme, especially one that allows for many more species of hydrometeors, may alleviate this problem.

Another parameterization that may be playing a significant role in creating errors in the microphysics fields is the planetary boundary layer (PBL) parameterization. The PBL parameterization calculates the surface fluxes and vertical mixing within the boundary layer, key processes that determine the structure and intensity of updrafts originating from the boundary layer. In the comparisons shown here, the significant increase of vertical motion with height just above the surface in the observations was not captured in the simulations (cf. Figs. 4 and 6). The weaker vertical gradient of vertical motion in the simulations implies weaker boundary layer convergence of high θ_e air at the surface in the

simulations and diminished upward heat and moisture transports in the eyewall, which may have an impact on determining the initial distribution and magnitude of vertical motion, humidity, and hydrometeor mixing ratio perturbations in the updrafts that drive the convection. The importance of the boundary layer parameterization in tropical cyclone simulations was also shown by Braun and Tao (2000), who found that the formulation of surface fluxes, as manifested by the calculation of surface exchange coefficients in the PBL parameterization, was the primary determinant of the intensity and precipitation structure in their MM5 simulations of Hurricane Bob (1991). Such a sensitivity indicates the likelihood that the PBL parameterization is a key player in determining the structure and intensity of convection in the model.

A possible source of error in the control simulation may also be related to continued inadequacies in the horizontal and vertical resolution of the model. The control simulation is capable of resolving much of the primary and secondary vortex-scale circulation, but it may not be adequately resolving the sharp gradients within the eyewall that play a role in governing the strength of these circulations. Also, the convective-scale vertical motions may be inadequately represented. For example, Jorgensen et al. (1985) found that 90% of the updrafts in a tropical cyclone they sampled had a diameter less than 4 km, corresponding to approximately $2\Delta x$ for the grid length of the control simulation, and nearly 50% of their updrafts were less than 2 km in diameter. This suggests that a sizable proportion of drafts are still not being resolved by the model at 1.67-km grid length. Furthermore, as shown in Bryan et al. (2003), simulations of squall lines with a grid length of 1 km were significantly different than simulations with a grid length of 125 m, with convective overturning in the 1-km simulation being much more laminar than the 125-m simulation. At 1-km grid length, updrafts can be artificially damped due to subgrid turbulence, and therefore may not be as strong and may not reach as high. Bryan et al. (2003) asserted that it is necessary to run models with a grid length on the order of 100 m for the subgrid-scale turbulence parameterization to perform appropriately. The vertical resolution may also be insufficient for resolving the strongest up- and downdrafts, particularly in the upper troposphere, where the vertical resolution is less than in the lower troposphere (see section 2).

6. Summary and concluding remarks

A methodology for evaluating microphysics fields from tropical cyclone simulations using Yuter and Houze (1995) CFAD diagrams, improved by implementing an objective hurricane partitioning technique, is demonstrated by comparing airborne observations of vertical motion and reflectivity from multiple tropical cyclones with cloud-scale numerical model simulations of two hurricanes. The ability to reliably evaluate microphysics fields from tropical cyclone simulations is an important task in formulating and testing any numerical modeling system. The evaluation methodology shown here illustrates several key differences in the microphysics fields between the simulations and the observations: weaker up- and downdrafts in the simulations than the observations, higher reflectivities in the simulations, a slower decrease of reflectivity with height above the melting level in the simulations, a narrower (broader) distribution of vertical motion (reflectivity) in the simulations, a narrowing of the vertical motion distribution with height in the simulations, and a much stronger correlation between the vertical motion and the hydrometeor mixing ratio/reflectivity in the simulations. The biases indicated by these evaluations could have important implications for the ability of high-resolution simulations to better predict tropical cyclone intensity and rainfall, since they may point to problems in obtaining accurate distributions of hydrometeors and their linkages with the vertical velocity field. Such linkages are crucial for obtaining accurate distributions of latent heating in time and space.

The biases shown here may be attributable to a variety of factors that can be divided into two major categories: differences in the way the data are processed from the observation and the simulation databases and deficiencies in the configuration of the simulations themselves. For Part I, attention focused on the possibility that the differences are due to differences in the way the data are processed and analyzed in the two databases, for example, inadequate reflectivity–mass relationships in the calculation of model reflectivity, uncertainties in the assumption of the hydrometeor fall speeds used to obtain vertical motion of the air, and differences in the horizontal resolution between the observation and simulation databases. Comparisons of analyses that account for these uncertainties indicate that they may explain some of the differences in the magnitudes of the fields, but the key differences between the databases remain. Thus data processing differences are likely not sufficient to explain the differences in the microphysics fields between the two databases. In Part II, attention will be focused on the possibility that the differences are due to deficiencies in the simulations. A variety of sensitivity tests will be performed to address the possibility that the differences in the microphysics fields are due to deficiencies in the planetary boundary layer and microphysical parameter-

izations and inadequate horizontal and vertical resolution. The same evaluation methodology will be used in Part II.

It is also possible that the inclusion of only two storms in the simulation database did not adequately cover the range of mature tropical cyclone strengths, sizes, and microphysics fields included in the observational database. The comparisons of the microphysics fields use statistical methods, involving the inclusion of 24 h of model output in the composites from the two simulations, which likely provided a sufficient range of conditions to produce a robust enough dataset for adequate comparisons with the observational database. Furthermore, the values of minimum sea level pressure in the simulations were well within the range of values of the majority of storms in the observational database (cf. Fig. 2 and Table 1). The inclusion of additional simulations of different storms is desirable, though, and is intended in future efforts. The inclusion of additional simulations (and observations) of tropical cyclones at different stages of their life cycle is also desirable, and it too is left for future work.

An interesting result from these comparisons is that even though the statistics describing the microphysics fields of the simulated storms were considerably different from the observations, the track and intensity of the simulated storms were reasonably well replicated (cf. Fig. 2). This suggests that, for these cases at least, accurately reproducing the microphysics fields is not crucial to obtaining accurate track and intensity forecasts. Much further testing, involving many more simulations of different storms, is required before this could be adequately addressed, however. Also, it is still likely that the ability to reproduce microphysics fields has a significant impact on the forecast of tropical cyclone rainfall.

There are many advantages to using the evaluation methodology shown here. First, because the comparisons are statistical in nature, they do not require a precise temporal and spatial matching of features between the observations and the simulations. This is advantageous, since it is beyond the current realm of predictability to be able to exactly reproduce the timing and location of vertical motion maxima/minima and convective and stratiform features. Another value to this evaluation technique is the fact that it is adaptable to a variety of observation platforms and model configurations. Additional observation platforms, such as Tropical Rainfall Measuring Mission precipitation radar (TRMM PR) reflectivity fields and NASA ER-2 Doppler radar (EDOP) vertical velocity and reflectivity fields from the NASA ER-2 aircraft, can easily be compared with the high-resolution simulations.

The evaluation technique shown here can also be used to evaluate the microphysics fields in operational models to highlight possible areas in need of improvement. Adding complexity to the parameterization schemes in the operational models may be impractical due to computational efficiency limitations and operational constraints, however, and it may actually add little to improve the forecasts. The evaluation methodology shown here has the potential of demonstrating the utility of implementing more complex parameterization schemes or higher resolution in the operational models. Such improved assessments could help to identify the optimal configuration of operational models to most faithfully reproduce microphysics fields from tropical cyclones and to determine the impact of improving these fields on forecasts of tropical cyclone intensity and rainfall.

Acknowledgments. Our thanks go to many people who helped in the preparation of this manuscript. Frank Marks and Paul Willis of HRD provided many helpful comments and suggestions to improve the work, as did Chris Landsea and Shirley Murillo, also of HRD. Scott Braun of NASA GSFC provided helpful suggestions and stimulating discussions about the use of microphysical parameterization schemes in hurricane environments. Our thanks also go to Nancy Griffin of HRD who provided radar images to us and to Joe Tenerelli, formerly of RSMAS/University of Miami, who was very helpful in providing assistance with the simulations. We also thank three anonymous reviewers whose careful and thoughtful suggestions significantly improved this manuscript. This work was partially supported by NOAA base funds and by a grant from NASA, Grant S-44774-X, as a part of the CAMEX-IV field program. This research was carried out (in part) under the auspices of the Cooperative Institute for Marine and Atmospheric Studies (CIMAS), a joint institute of the University of Miami and NOAA, Cooperative Agreement NA67RJ0149.

APPENDIX

Classification Algorithm for Eyewall, Rainband, and Stratiform Regions

Reflectivity is first averaged in two layers, the 0.5–4-km layer (lower-level reflectivity) and the 6–10-km layer (upper-level reflectivity). Figure A1 provides a radius–height schematic of the reflectivity fields in a mature hurricane [based on observational studies, such as Jorgensen (1984) and Marks and Houze (1987)] and the definition of the candidate regions. The eyewall candidate region is identified first. Starting from the

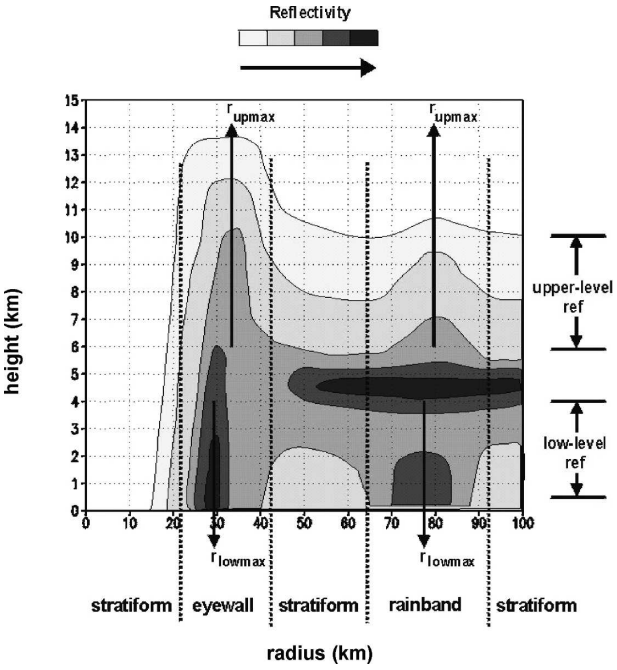

FIG. A1. Schematic showing identification of candidate eyewall, rainband, and stratiform regions based on reflectivity.

center of the grid (i.e., the center of the simulated or observed storm), the upper-level reflectivity is evaluated until the first instance where it exceeds 30 dBZ. From this point, the upper-level reflectivity is evaluated for an additional 15 km. The maximum upper-level reflectivity within this radial band is flagged (r_{upmax}). The lower-level reflectivity is then evaluated in a 20-km radial band centered on the flagged point, and the maximum low-level reflectivity is saved and the radius corresponding to that value is flagged (r_{lowmax}). Moving radially outward from r_{upmax}, the upper-level reflectivity is evaluated until it falls below 70% of the value at r_{upmax}. Additionally, the lower-level reflectivity is evaluated until it falls below 70% of the value at r_{lowmax}. The maximum of these two radii is defined as the outer edge of the eyewall candidate region. Moving radially inward from r_{lowmax}, the lower-level reflectivity is evaluated until it falls below 15 dBZ. This radius is defined as the inner edge of the eyewall candidate region.

Moving radially outward from the eyewall, the rainband candidate regions are next identified. This technique uses nearly the same algorithm as the eyewall determination, with a few minor differences: 1) the initial reflectivity used to flag a possible rainband is 25 dBZ instead of 30 dBZ; 2) only one test is performed to identify the outer edge of the rainband; 3) because of weaker radial gradients in reflectivity at larger radii, the threshold value to identify the outer edge of a rainband is 75% instead of 70% of the maximum upper-level reflectivity; and 4) the criterion for defining the inner edge of a rainband is when the low-level reflectivity falls below 75% of the maximum lower-level reflectivity (rather than a 15-dBZ threshold for the eyewall inner edge).

To identify a stratiform region, all locations that are neither eyewall nor rainband, but where the lower-level reflectivity exceeds 15 dBZ, are considered stratiform regions. All other regions are considered "other," unless the lower-level reflectivity is below 2 dBZ, in which case it is considered to be missing. Because of the high bias of simulated reflectivities when compared to observations (cf., e.g., Fig. 1), the thresholds used to define a potential eyewall and rainband (30 and 25 dBZ, respectively) are reduced by 5 dBZ for the observed data.

With the candidate regions identified from the reflectivity fields (Fig. A1), the vertical motion fields are next used to identify the actual eyewall, rainband, and stratiform regions. To preserve radial contiguity, the absolute values of vertical motion in the layer between 4 and 10 km are averaged over a 5-km radial distance. If the running mean of vertical motion anywhere within a 5-km distance of the location being considered is greater then 1.5 m s^{-1} within a candidate eyewall (or rainband) region, then that location is identified as part of the eyewall (or rainband). The value of 1.5 m s^{-1} is chosen because that value was found in Black et al. (1996) to define the boundaries of coherent up- and downdrafts in their VI dataset. If no region within 5 km is greater than 1.5 m s^{-1}, that location is considered stratiform.

REFERENCES

Barnes, G. M., and M. D. Powell, 1995: Evolution of the inflow boundary layer of Hurricane Gilbert (1988). *Mon. Wea. Rev.,* **123,** 2348–2368.

Black, M. L., R. W. Burpee, and F. D. Marks Jr., 1996: Vertical motion characteristics of tropical cyclones determined with airborne Doppler radial velocities. *J. Atmos. Sci.,* **53,** 1887–1909.

Black, R. A., 1990: Radar reflectivity-ice water content relationships for use above the melting level in hurricanes. *J. Appl. Meteor.,* **29,** 955–961.

——, and J. Hallett, 1986: Observations of the distribution of ice in hurricanes. *J. Atmos. Sci.,* **43,** 802–822.

——, H. B. Bluestein, and M. L. Black, 1994: Unusually strong vertical motions in a Caribbean hurricane. *Mon. Wea. Rev.,* **122,** 2722–2739.

——, G. M. Heymsfield, and J. Hallett, 2003: Extra large particle images at 12 km in a hurricane eyewall: Evidence of high-altitude supercooled water? *Geophys. Res. Lett.,* **30,** 2124, doi:10:1029/2003GF017864.

Blackadar, A. K., 1979: High resolution models of the planetary boundary layer. *Advances in Environmental Science and En-*

gineering, Vol. 1, J. Pfafflin and E. Ziegler, Eds., Gordon and Breach Science, 50–85.

Braun, S. A., 2002: A cloud-resolving simulation of Hurricane Bob (1991): Storm structure and eyewall buoyancy. *Mon. Wea. Rev.,* **130,** 1573–1592.

——, and R. A. Houze Jr., 1994: The transition zone and secondary maximum of radar reflectivity behind a midlatitude squall line: Results retrieved from Doppler radar data. *J. Atmos. Sci.,* **51,** 2733–2755.

——, and W.-K. Tao, 2000: Sensitivity of high-resolution simulations of Hurricane Bob (1991) to planetary boundary layer parameterizations. *Mon. Wea. Rev.,* **128,** 3941–3961.

Bryan, G. H., J. Wyngaard, and J. M. Fritsch, 2003: Resolution requirements for the simulation of deep moist convection. *Mon. Wea. Rev.,* **131,** 2394–2416.

Cangialosi, J., and S. S. Chen, 2004: A numerical study of the topographic effects on structure and rainfall in Hurricane Georges (1998). Preprints, *26th Conf. on Hurricanes and Tropical Meteorology,* Miami, FL, Amer. Meteor. Soc., CD-ROM, 13D.4.

Davis, C., and L. F. Bosart, 2002: Numerical simulations of the genesis of Hurricane Diana (1984). Part II: Sensitivity of track and intensity prediction. *Mon. Wea. Rev.,* **130,** 1100–1124.

DeMaria, M., and J. M. Gross, 2003: Evolution of prediction models. *Hurricane! Coping with Disaster,* R. Simpson, Ed., Amer. Geophys. Union, 103–126.

Dudhia, J., 1989: Numerical study of convection observed during the Winter Monsoon Experiment using a mesoscale two-dimensional model. *J. Atmos. Sci.,* **46,** 3077–3107.

Farley, R. D., 1987: Numerical modeling of hailstorms and hailstone growth. Part III: Simulation of an Alberta hailstorm—Natural and seeded cases. *J. Appl. Meteor.,* **26,** 789–812.

Ferrier, B. S., W.-K. Tao, and J. Simpson, 1995: A double-moment multiple-phase four-class bulk ice scheme. Part II: Simulations of convective storms in different large-scale environments and comparisons with other bulk parameterizations. *J. Atmos. Sci.,* **52,** 1001–1033.

Fovell, R. G., and Y. Ogura, 1988: Numerical simulation of a midlatitude squall line in two dimensions. *J. Atmos. Sci.,* **45,** 3846–3879.

Grell, G. A., J. Dudhia, and D. R. Stauffer, 1994: A description of the fifth generation Penn State/NCAR Mesoscale Model (MM5). NCAR Tech. Note NCAR/TN-398+STR, 138 pp.

Jorgensen, D. P., 1984: Mesoscale and convective-scale characteristics of mature hurricanes. Part II: Inner core structure of Hurricane Allen (1980). *J. Atmos. Sci.,* **41,** 1287–1311.

——, and M. A. LeMone, 1989: Vertical velocity characteristics of oceanic convection. *J. Atmos. Sci.,* **46,** 621–640.

——, E. J. Zipser, and M. A. Lemone, 1985: Vertical motions in intense hurricanes. *J. Atmos. Sci.,* **42,** 839–856.

——, T. J. Matejka, D. Johnson, and M. A. LeMone, 1994: A TOGA-COARE squall line seen by multiple airborne Doppler radars. Preprints, *Sixth Conf. on Mesoscale Processes,* Portland, OR, Amer. Meteor. Soc., 25–28.

Kain, J. S., and J. M. Fritsch, 1993: Convective parameterization for mesoscale models: The Kain–Fritsch scheme. *The Representation of Cumulus Convection in Numerical Models, Meteor. Monogr.,* No. 46, Amer. Meteor. Soc., 165–170.

Karyampudi, V. M., G. S. Lai, and J. Manobianco, 1998: Impact of initial conditions, rainfall assimilation, and cumulus parameterization on simulations of Hurricane Florence (1988). *Mon. Wea. Rev.,* **126,** 3077–3101.

Lawrence, M. B., L. A. Avila, J. L. Beven, J. L. Franklin, J. L. Guiney, and R. J. Pasch, 2001: Atlantic hurricane season of 1999. *Mon. Wea. Rev.,* **129,** 3057–3084.

Lin, Y.-L., R. D. Farley, and H. D. Orville, 1983: Bulk parameterization of the snow field in a cloud model. *J. Climate Appl. Meteor.,* **22,** 1065–1092.

——, D.-L. Zhang, and M. K. Yau, 1997: A multiscale numerical study of Hurricane Andrew (1992). Part I: Explicit simulation and verification. *Mon. Wea. Rev.,* **125,** 3073–3093.

Marchok, T., R. Rogers, and R. Tuleya, 2007: Validation schemes for tropical cyclone quantitative precipitation forecasts: Evaluation of operational models for U.S. landfalling cases. *Wea. Forecasting,* in press.

Marks, F. D., and R. A. Houze Jr., 1987: Inner core structure of Hurricane Alicia from airborne Doppler radar observations. *J. Atmos. Sci.,* **44,** 1296–1317.

——, ——, and J. F. Gamache, 1992: Dual-aircraft investigation of the inner core of Hurricane Norbert. Part I: Kinematic structure. *J. Atmos. Sci.,* **49,** 919–942.

McFarquhar, G. M., and R. A. Black, 2004: Observations of particle size and phase in tropical cyclones: Implications for mesoscale modeling of microphysical processes. *J. Atmos. Sci.,* **61,** 422–439.

Olson, W. S., C. D. Kummerow, Y. Hong, and W.-K. Tao, 1999: Atmospheric latent heating distributions in the Tropics derived from satellite passive microwave radiometer measurements. *J. Appl. Meteor.,* **38,** 633–664.

Orville, H. D., and F. J. Kopp, 1990: A numerical simulation of the 22 July 1979 HIPLEX-1 Case. *J. Appl. Meteor.,* **29,** 539–550.

——, R. D. Farley, and J. H. Hirsch, 1984: Some surprising results from simulated seeding of stratiform-type clouds. *J. Appl. Meteor.,* **23,** 1585–1600.

Pagowski, M., and G. W. K. Moore, 2001: A numerical study of an extreme cold-air outbreak over the Labrador Sea: Sea ice, air–sea interaction, and development of polar lows. *Mon. Wea. Rev.,* **129,** 47–72.

Pasch, R. J., L. A. Avila, and J. L. Guiney, 2001: Atlantic hurricane season of 1998. *Mon. Wea. Rev.,* **129,** 3085–3123.

Powell, M. D., 1990a: Boundary layer structure and dynamics in outer hurricane rainbands. Part I: Mesoscale rainfall and kinematic structure. *Mon. Wea. Rev.,* **118,** 891–917.

——, 1990b: Boundary layer structure and dynamics in outer hurricane rainbands. Part II: Downdraft modification and mixed layer recovery. *Mon. Wea. Rev.,* **118,** 918–938.

Rogers, R. F., S. S. Chen, J. E. Tenerelli, and H. E. Willoughby, 2003: A numerical study of the impact of vertical shear on the distribution of rainfall in Hurricane Bonnie (1998). *Mon. Wea. Rev.,* **131,** 1577–1599.

Smagorinsky, J., S. Manabe, and J. L. Holloway, Jr., 1965: Numerical results from a nine-level general circulation model of the atmosphere. *Mon. Wea. Rev.,* **93,** 727–768.

Smith, P. L., Jr., C. G. Myers, and H. D. Orville, 1975: Radar reflectivity factor calculations in numerical cloud models using bulk parameterization of precipitation. *J. Appl. Meteor.,* **14,** 1156–1165.

Tao, W.-K., and J. Simpson, 1993: The Goddard cumulus ensemble model. Part I: Model description. *Terr. Atmos. Oceanic Sci,* **4,** 35–72.

——, and Coauthors, 2001: Retrieved vertical profiles of latent heat release using TRMM rainfall products for February 1998. *J. Appl. Meteor.,* **40,** 957–982.

Tenerelli, J. E., and S. S. Chen, 2002: Intensity change and eyewall replacement in Hurricane Floyd (1999). Preprints, *25th Conf. on Hurricanes and Tropical Meteorology,* San Diego, CA, Amer. Meteor. Soc., 168–169.

——, and ——, 2004: Influence of initial vortex structure on the simulation of hurricane lifecycles. Preprints, *26th Conf. on Hurricanes and Tropical Meteorology,* Miami, FL, Amer. Meteor. Soc., CD-ROM, 15C.3.

Turpeinen, O., and M. K. Yau, 1981: Comparisons of results from a three-dimensional cloud model with statistics of radar echoes on Day 261 of GATE. *Mon. Wea. Rev.,* **109,** 1495–1511.

Weisman, M. L., W. C. Skamarock, and J. B. Klemp, 1997: The resolution dependence of explicitly modeled convective systems. *Mon. Wea. Rev.,* **125,** 527–548.

Willis, P. T., and D. P. Jorgensen, 1981: Reflectivity relationships for hurricanes. Preprints, *20th Conf. on Radar Meteorology,* Boston, MA, Amer. Meteor. Soc., 85–90.

Willoughby, H. E., 1995: Mature structure and evolution. *Global Perspectives on Tropical Cyclones,* WMO Tech. Doc. 693, R. L. Elsberry, Ed., WMO, 21–62.

Yuter, S. E., and R. A. Houze Jr., 1995: Three-dimensional kinematic and microphysical evolution of Florida cumulonimbus. Part III: Vertical mass transport, mass divergence, and synthesis. *Mon. Wea. Rev.,* **123,** 1964–1983.

Zhang, D.-L., and R. A. Anthes, 1982: A high-resolution model of the planetary boundary layer–sensitivity tests and comparisons with SESAME-79 data. *J. Appl. Meteor.,* **21,** 1594–1609.

——, Y. Liu, and M. K. Yau, 2000: A multiscale numerical study of Hurricane Andrew (1992). Part III: Dynamically induced vertical motion. *Mon. Wea. Rev.,* **128,** 3772–3788.